FEATURE ARTICLE

Physics of the Switching Kinetics in Resistive Memories

Stephan Menzel, Ulrich Böttger, Martin Wimmer, and Martin Salinga*

Memristive cells based on different physical effects, that is, phase change, valence change, and electrochemical processes, are discussed with respect to their potential to overcome the voltage–time dilemma that is crucial for an application in storage devices. Strongly non-linear switching kinetics are required, spanning more than 15 orders of magnitude in time. Temperature-driven and field-driven crystallization, threshold switching, ion migration, as well as redox reactions at interfaces are identified as relevant mechanisms. In phase change materials the combination of a reversible threshold switching and extremely large crystal growth velocities at high voltages enables ultra-fast resistive switching whereas lower voltages will not be sufficient to overcome the energy barrier for crystallization. In electrochemical cells it depends on the voltage regime, which mechanism is the rate-determining one for switching. While electro-crystallization dominates at low voltages, electron transfer in the medium voltage range and a mixture of electron transfer and ion migration at high voltages. In valence change materials, ion migration is found to be accelerated by a combined effect of electric field and local temperature increase due to Joule heating. All discussed types of resistive switches can provide sufficient non-linearity of switching kinetics for overcoming the voltage time dilemma.

1. Introduction

As conventional memory devices are approaching their scaling limits, non-volatile resistive switching devices attract great attention for their utilization in resistive random access memories (RRAM).[1–5] In a resistive memory the different memory states are accessed by a resistive non-destructive read-out. Among the various types of resistive switching devices, redox-based resistive memories (ReRAM) based either on a valence change mechanism (VCM) or on an electrochemical mechanism (ECM) and also phase change memory (PCM) show very promising properties: non-volatility, fast device operation (<10 ns),[6–9] and high endurance (>10^{10} cycles).[10–13] The write energy of these devices is typically in the range of hundreds of fJ to a few pJ and thus higher as in a conventional dynamic random access memory (DRAM). However, in memory concepts that capitalize on the non-volatility of the resistive devices the overall energy consumption during operation is much lower. In addition, the energy consumption for nanometer-sized devices will be more and more dominated by the charging of the memory array itself.[14,15] While phase change memories are already in the market since 2009 (512Mb PRAM by Samsung),[16] the first product based on TaO_x-based VCM cells has been released in 2013 by Panasonic[17] and large-scale ECM memory prototypes have been demonstrated recently.[18] In addition to the memory application, ECM, VCM and PCM devices offer the potential for realization of logic-in-memory concepts.[19–22] Such concepts can overcome the limitations of the conventional von Neumann computing paradigm.

In order to meet the requirements for a competitive non-volatile memory, on the one hand a resistive switch needs to switch as fast as some nanoseconds when electrically excited with only a few volts. On the other hand the resistance state should not change while applying a read voltage of few hundred mV for up to ten years. This combination of fast switching and immunity to long-lasting read-disturb is also known as voltage-time dilemma.[1] In order to fulfill both requirements in one device its switching kinetics should exhibit a non-linearity that is large enough to span over these more than 15 orders of magnitude in time. This is a maximum requirement due to the fact that a memory cell is not read out continuously. To achieve a very high non-linearity, the development of a general understanding of the electrochemical and physical processes that determine the switching kinetics of PCM, VCM and ECM devices is one of the most relevant research tasks. In particular, the question arises how the voltage-time dilemma can be solved for a specific type of resistively switching devices.

In this paper we first give a basic overview of the potential switching mechanisms. Then, we describe in more detail how physical and electrochemical processes can limit the switching speed and discuss their non-linearity. Finally, we consider experimental observations in those three types of resistive memory devices.

Dr. S. Menzel
Peter Grünberg Institute (PGI-7)
Research Center Jülich
52425 Jülich, Germany
E-mail: st.menzel@fz-juelich.de
Dr. U. Böttger
Institute of Materials in Electrical Engineering and Information Technology II
RWTH Aachen University
52056 Aachen, Germany
Dr. M. Wimmer, Dr. M. Salinga
I. Physikalisches Institut 1A
RWTH Aachen University
52056 Aachen, Germany

DOI: 10.1002/adfm.201500825

2. Physical Switching Principle of Resistive Memories

PCM, VCM, and ECM devices can be switched repetitively between a high resistance state (HRS) and a low resistance state (LRS). Thereby, the transition from HRS to LRS is called SET operation and the reverse operation RESET. Moreover, it is possible to switch into intermediate resistance states and hence storing more than one bit in a single cell is attainable. In a PCM device SET and RESET operation can be performed with the same voltage polarity, that is, unipolar operation. In contrast, the SET and RESET operation in ECM and VCM cells require opposite voltage polarities, so-called bipolar operation.

2.1. Phase Change Memories

Prominent materials for prototype phase change memory devices can be found on the pseudo-binary line between GeTe and Sb_2Te_3. Beside these commonly used compounds, also stoichiometries like doped Sb_2Te, $Ge_{15}Sb_{85}$ or even pure antimony show a pronounced contrast in their electrical properties as well as fast switching kinetics.[23,24] For electrical data storage applications the strong contrast in resistivity between the crystalline (LRS) and the amorphous phase (HRS) of up to 4 orders of magnitude is used to define logical states.[25,26]

In order to guarantee fast SET and RESET speeds the reversible transition between the two phases has to be performed within a few nanoseconds. During RESET the conductive crystalline phase change material is locally heated (via Joule heating) above the melting temperature and subsequently cooled down. Due to the thermal design of phase-change memory devices (i.e., the thermal conductivity of the surrounding materials and the large surface-to-volume ratio) high cooling rates (10^9–10^{11} K/s) are realized.[27] This way, the atomically disordered liquid material is melt-quenched, resulting in an amorphous solid state. While the duration of the RESET process is mainly controlled by the thermal time constant of a phase change memory cell and especially its surrounding rather than by the phase change material itself, it is the SET operation, that is, the crystallization, in which the write speed is crucially limited by fundamental properties of the chosen phase change material.[28–32] For the SET process the temperature within the amorphous material is locally raised (again via Joule heating) above the glass transition temperature. At these elevated temperatures crystallization of the amorphous matrix occurs via spontaneous creation of crystalline nuclei (nucleation) and via growth of existing crystal grains. Which of the two mechanisms dominates the overall crystallization, strongly depends on the local temperature, the given volume and boundary conditions.[33–35] For example, due to the existence of a crystalline surrounding around an amorphous volume, as it is commonly found in vertical memory cell geometries, fast re-crystallization is possible via crystal growth alone, without the need to wait for spontaneous nucleation. Then again, Loke et al. presented a crystallization speed of 500 ps in $Ge_2Sb_2Te_5$ when superimposing a constant low voltage signal with the SET pulse.[36] The extremely fast phase transition in this work was explained by pre-ordering effects under applied bias. Although one of the crystallization mechanisms might dominate under specific boundary conditions, in general both nucleation and crystal growth are present during crystallization.

A recent study on the crystal growth velocity in melt-quenched amorphous AgIn-doped Sb_2Te revealed an Arrhenius

Stephan Menzel is a senior scientist at the Peter Grünberg Institute (PGI-7), Research Center Juelich. He studied electrical engineering at RWTH Aachen and received his diploma degree in 2006 and afterwards his Ph.D. in 2012. During his doctor thesis he was concerned with the modeling and simulation of resistive switching devices. Since 2012, Stephan Menzel is the head of the simulation group at PGI-7.

Ulrich Böttger received his diploma degree in physics in 1888 and the Dr.-Ing. degree in 1994, both from the Rheinisch-Westfälische Hochschule (RWTH) Aachen. After 4 years as project manager of SMEs he joined RWTH Aachen again working in the fields of "ferroelectric and dielectric devices" as well as "resistive switching devices" at the Institute of Electroceramic Materials (IWE 2). He is author and co-author of more than 100 scientific papers.

Martin Salinga is an academic staff member of the department of physics at RWTH Aachen University, Germany. After two years of research in the USA, at Harvard University and the IBM Almaden Research Center, he returned to his alma mater, RWTH, at the end of 2006. After receiving his doctoral degree in physics from RWTH in 2008 he accepted a permanent position there as a research team leader. Since July 2011 he is principal investigator and member of the steering committee of the collaborative research center "Nanoswitches". In his research he concentrates on resistive switching and dynamics of amorphous semiconductors.

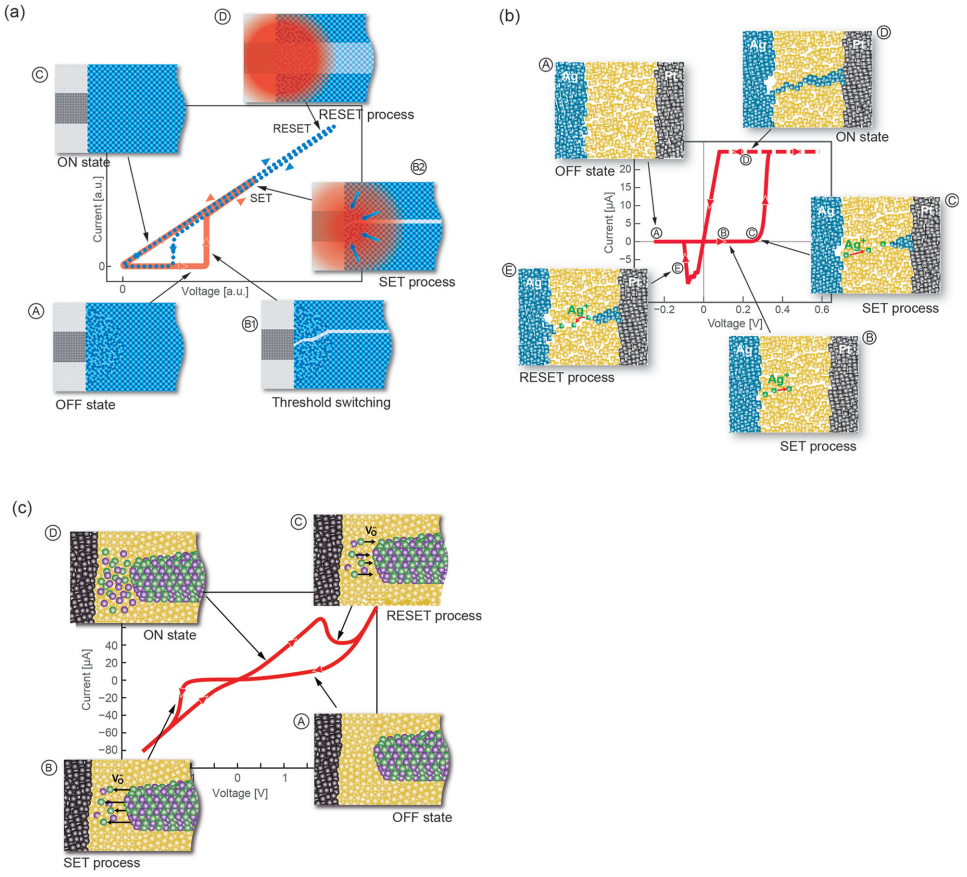

Figure 1. Illustration of the different switching principles with corresponding *I–V* characteristics: a) The SET process of phase-change memory cell (PCM) is correlated with two steps. Firstly, the reversible reduction in resistivity at the threshold voltage (B1), indicated by a reversible increase of the current, leads to an increase of the local temperature in the phase-change nano-structure via Joule-heating facilitating in a second step the crystallization of the intial amorphous phase-change material (B2). This change of the cell state is irreversible, that is, after reducing the applied bias the cell resistance remains low (C). The RESET process is triggered by applying an intense voltage pulse, which raises the local temperature above the melting temperature and partially melt the crystalline cell (D). The subsequent rapid quenching of the device freezes the atoms in a disordered configuration resulting in an amorphous solid with a high resistivity. b) By applying a positive voltage to the active electrode of an electrochemical metallization cell (ECM), an oxidation reaction occurs at the active electrode/insulating layer interface. Then, the injected Cu or Ag ions migrate within the electric field through the insulating layer (B). At the inert electrode/insulating layer interface another electron-transfer reaction occurs. The Cu/Ag ions are reduced and a Cu/Ag filament starts to grow towards the anode after having formed a stable Cu/Ag nucleus (C). c) When a negative voltage is applied to the active electrode, oxygen vacancies migrate towards this electrode (B). Hence, the insulating region between the substoichiometric well – conducting filament and the active electrode becomes conducting and the VCM cell switches to the LRS (C). By reversing the voltage – polarity oxygen vacancies are pushed back from the active electrode (D) and finally the HRS is reestablished (A). (b,c) are reproduced with permission.[81] Copyright 2012, Wiley-VCH.

behavior over 8 orders of magnitude.[37] Also Orava et al. measured a strongly non-linear temperature dependence of the crystal growth velocity in $Ge_2Sb_2Te_5$ using ultra-fast differential scanning calorimetry.[38] The strong non-linearity in crystallization kinetics thereby provides good data retention at low temperatures as well as fast switching speeds (crystal growth velocity of ≈1 m/s) at elevated temperatures between glass transition and melting temperature.

Another key feature in amorphous PCM that helps to overcome the voltage-time dilemma is the pronounced non-linearity of the current–voltage characteristics, most importantly the "threshold switching" phenomenon (see **Figure 1**a). With a linear current–voltage relationship, sufficiently strong Joule heating would require extremely large voltages, due to the low conductivity of the amorphous phase. In reality, however, the current follows the applied voltage linearly only at low electric field strengths. Already under medium electric fields an exponential current–voltage-dependence sets in. In literature, this behavior is often attributed to the large concentration of defects and the field-induced reduction in Coulomb-barrier described by the Poole- and Poole-Frenkel effect in the amorphous phase.[39,40] A further increase in electrical field leads to a super-exponential *I–V* characteristic, which ends in an abrupt breakdown in resistivity, the threshold switching phenomenon. The threshold switching effect thereby describes the transition from the poorly conductive (off-state) to the highly conductive amorphous phase (on-state). Thus, the thermally driven crystallization of the amorphous material (SET) is triggered by the threshold-switching event. In PCM the strong non-linearity in switching behavior can therefore be understood as a cooperative effect between the threshold switching phenomenon and the exceptional crystallization kinetics.

2.2. Electrochemical Metallization Memories

ECM cells consist of one active silver or copper electrode an ion-conducting insulating layer and an inert electrode.[2,41] Thereby, solid electrolytes such as GeS_x,[42,43] GeSe,[11,44] or AgI,[45,46] or metal oxides such as Ta_2O_5[47] or SiO_2[48,49] can serve as ion-conducting layer. The resistive switching mechanism in ECM cells is based on the electrochemical formation/dissolution of a Ag/Cu filament within the insulating layer.[2,41,50] The SET process consists of a dissolution of the active anodic Ag or Cu electrode, a subsequent ion migration and a reduction at the cathode resulting in a growth of a metallic filament towards the anode as illustrated in Figure 1b. As soon as an electronic contact is achieved, the cell resistance drops to the LRS. For this reason, ECM cells are also widely known as Conductive Bridging Random Access Memories (CBRAM).[51] Typically, pristine ECM cells do not require a special electroforming step for successful operation.

The electronic contact can be achieved by the onset of electron tunneling between the filament and the active electrode. By tuning the current limitation during the SET operation different LRS can be programmed.[49,51,52] These different resistance states can be attributed to different tunneling gaps in the range of 0.3 nm to 2 nm between the filament tip and the active electrode.[53] When the current compliance is further increased the gap can be shortened establishing a galvanic contact with a lower LRS resistance. Further LRS resistance reduction might result from a filament diameter widening.[53] It is experimentally observed that quantized conduction states appear for resistances below the resistance of a single-atom contact $R_0 = 12.9\ k\Omega$,[45,54–56] which is an indirect proof of the transition between tunneling gap regime and galvanic contact. Furthermore, it has been reported that the RESET transition can be polarity-independent in the low resistance regime,[57–60] whereas it is always bipolar for resistances $R > R_0$.

To RESET the cell back to the HRS state a negative voltage must be applied to the active electrode and the filament is dissolved. Depending on the physical nature of the LRS the dissolution of the filament takes place in slightly differing ways. If a tunneling gap remains in the LRS, the RESET operation involves the same processes as the SET operation, only the role of the electrodes is interchanged—the inert electrode becomes the anode, the active electrode the cathode. Of course, a nucleation step is not required for the RESET operation. If a galvanic contact has formed during SET, the RESET process starts with a pinching of the filament. This effect has been experimentally observed using conductive atomic force microscope (c-AFM) tomography by Celano et al.[61,62] Due to the high currents in this configuration also Joule heating occurs with the hot spot at the weakest spot within the filament, for example, for a conically shaped filament at the thinner side. As the electron-transfer reactions are thermally enhanced, both the oxidation of the filament and the redeposition (reduction) occur close to this hot spot at the filament. Thus the filament reshapens in such a way that it pinches where the oxidation takes place.[60] As both reactions occur at the filament a RESET operation is feasible for both voltage polarities, but still the bipolar operation leads to more stable switching.[57,60]

The charge state of the cations is not always obvious. For a Ag ion the charge state is +1, whereas for Cu ions the charge state could be +1 or +2 depending on the specific system. In the Cu_2S system the charge state is +1 due to its bond nature. In contrast the charge state in the other materials SiO_2, Ta_2O_5, a-Si, and Al_2O_3 cannot be easily foreseen. It depends for example on the ease of injecting a specific sort of ions from the active electrode into the switching layer, that is, the oxidation reaction. Furthermore also the mobility of the charged species within the switching layer is important. Cyclic voltammetry experiments in the preforming stage of $Cu/SiO_2/Pt$ cells revealed that Cu^{1+} and Cu^{2+} ions can be injected but the dominating species is Cu^{2+}.[63] Using soft X-ray absorption spectroscopy the bonding characteristics of Cu^{z+} ions in SiO_2 have been analyzed by Cho and co-workers.[64] The analysis reveals that Cu^{2+} ions form weaker bonds than Cu^{1+} suggesting that Cu^{2+} ions are more mobile and play the dominating role in the resistive switching in Cu/SiO_2 ECM systems.

A very important variant of the ECM switching principle is the gap-type atomic switch.[65] In this variant an air(vacuum)-gap exists between the ion conductor and the inert electrode. This can be achieved using an STM tip in non-contact mode[66–68] or by an electroforming process in a nano-crosspoint configuration.[65] In contrast to the standard ECM cell, the cations cannot migrate through the air gap to the inert electrode. Instead the Ag or Cu cations at the ion conductor surface are reduced by tunneling electrons forming a small nucleus, further ions drift towards the nucleus and subsequently a filament grows from the surface to the inert electrode. This kind of growth mode from anode to cathode has been also observed by c-AFM tomography for a $Cu/Al_2O_3/TiN$ based ECM cell[61] or using in situ TEM in a $Ag/SiO_2/W$ ECM cell.[69] Yang et al. could demonstrate that the growth direction is in fact dominated by the kinetic factors of the filament formation.[69] If the cation mobility is high the conventional growth mode from cathode to anode occurs. In contrast, the growth from anode to cathode is favored, if the ion transport is very low. The latter condition is fulfilled for gap-type atomic switch.

2.3. Valence Change Memories

VCM cells consist of a metal-insulator-metal (MIM) structure. As insulator-layer various oxide materials have been investigated such as strontium titanate (STO),[70–72] titanium oxide (TiO_x),[73,74] hafnium oxide (HfO_x),[75,76] and tantalum oxide (TaO_x).[7,12] The latter two are regarded as the most promising materials, not least because of their CMOS compatibility. Apart from a single oxide layer, bilayer or multilayer stacks consisting of different materials have been investigated, too.[12,77,78]

It is widely accepted that the switching mechanism of VCM cells is based on the movement of oxygen ions in terms of a vacancy transport mechanism accompanied by a local valence change.[1,3,79,80] This can influence the cell resistance in different ways. First, the local conductivity/electron transport mechanism of the material itself is changed. Second, oxygen vacancies act as mobile donors. If the oxygen vacancy concentration at a metal/insulator interface is changed, the electrostatic barrier is altered according to the Schottky effect.[1,79,81]

Pristine cells typically need an electroforming step which makes the switching between ON and OFF possible. During this step the oxide material is reduced resulting in a better

conducting state which may be the HRS or LRS. Electroforming is regarded as a complex redox reaction of simultaneously occurring processes.[1,70,82] Oxygen is extracted from the insulating layer at the anode leaving oxygen vacancies behind. This oxidation reaction manifests either in an oxidation of the anode metal or in the release of gaseous oxygen. The corresponding reduction reaction takes place by the local valence change in the metal cation sublattice. The charged oxygen vacancies migrate through the insulating layer in the direction of the electric field and pile up at the cathode interface. The resulting oxygen-deficient region is well-conducting and acts as a virtual cathode. This typically filamentary region grows towards the anode. Up to now it is not clear whether this region is merely oxygen-deficient without changing the material structure or if an additional phase transition occurs. For example, Kwon et al. observed that Ti_4O_7 Magnèli phases have formed within a TiO_2 matrix after unipolar switching by TEM analyses.[83] Recently, Kamaladasa et al. observed the formation of Wadsley defects and Magnèli phases during resistive switching in TiO_2 based VCM cells using in situ TEM imaging.[84] However, Magnèli phase formation was only observed at elevated temperatures and not during bipolar operation. In addition, the formation/dissolution did not appear to correlate to the resistive switching phenomena at all. Nevertheless, if a phase transition occurs, a nucleation step is required before the new phase can grow.

For the sake of completeness, it should be noted that in case of HfO_x-based VCM cells, an alternative model has been proposed in which oxygen vacancies are formed not at the interface with the anode but by breaking Hf-O bonds within the bulk of the oxide layer.[85–87] This process creates a Frenkel defect pair consisting of an interstitial oxygen ion and an oxygen vacancy. In this model the interstitial oxygen ion is mobile whereas the oxygen vacancy is assumed to be immobile. In the end also an oxygen-deficient phase is formed. However, it has been shown by theoretical calculations that this sort of Frenkel defects are thermodynamically unstable in HfO_2; the oxygen ion would relax to its equilibrium position kinetically unhindered within a time scale of phonon frequencies.[88] Moreover, it was shown that it is thermodynamically favorable to form an oxygen vacancy at an Hf/HfO_2 interface rather than in the bulk.[88,89]

After the forming process two different proposed switching mechanisms can be discriminated. In the first one the SET process is considered to be a mere completion of what happens during the electroforming of the filament employing the same microscopic processes. In this case, the filament is oxidized during the RESET operation and a reduction reaction occurs at the cathode. This means the amount of oxygen vacancies within the film varies during switching by oxygen exchange via the active electrode.[86,90,91] The second proposed mechanism relies on the redistribution of oxygen vacancies next to the active electrode during the switching process as illustrated in Figure 1c.[1,79] In this case the total amount of oxygen vacancies stays constant.

3. Underlying Physical Processes of the Non-Linear Resistive Switching

In order to understand the non-linear switching kinetics of PCM, VCM, and ECM cells one has to consider all electrochemical and physical processes that can influence the switching speed. According to the switching mechanisms described above the most relevant processes are: i) crystallization including nucleation and growth of a new phase, ii) threshold switching, iii) the migration of ions, iv) electron-transfer (redox) reactions taking place at the boundaries, and v) electro-crystallization. The latter three are most relevant for ECM and VCM, while processes (i) and (ii) typically dominate in PCM cells. However, also for VCM cells phase transitions have been described in literature to occur during electroforming, for example, the formation of the Magnèli phase Ti_4O_7 in TiO_2.[83] However, prior to this process the oxide has to be reduced by means of oxygen vacancy migration.

3.1. Crystallization

The collective process of crystallization in phase-change materials has been successfully described by the interplay of atomic mobility and driving force for crystallization (see **Figure 2**). For temperatures close to the glass transition temperature T_g the driving force $\Delta G(T)$ is large, while the atomic mobility is low hindering the crystallization process. This way, the small mobility is the reason for high data retention in phase-change memories at low temperatures, that is, ambient/operating temperature of the device. In this regime the slow processes of nucleation and growth are easily accessible experimentally, for example, by transmission electron or atomic force microscopy.[92–94] At temperatures close to the liquidus temperature T_l the driving force vanishes. Therefore, the crystallization is also suppressed very close to the melting point despite the fact that the atomic mobility is extremely high. The technologically relevant fast switching in phase-change memories can be realized in the regime of fast crystallization between T_g and T_l, where the atomic mobility is very high and the driving force still significant.

3.1.1. Growth of a Crystallite

In the framework of classical crystallization theory the temperature dependence of the crystal growth velocity $u(T)$ can be described as

$$u(T) \propto D(T) \cdot \left(1 - \exp\left(-\frac{\Delta G(T)}{k_B T}\right)\right) \quad (1)$$

The difference in Gibbs free energy between the liquid and crystal phase can be calculated using the Thompson-Spaepen approximation[95]

$$\Delta G(T) = \Delta H_m \frac{T_m - T}{T_m}\left(\frac{2T}{T_m + T}\right) \quad (2)$$

with heat of fusion ΔH_m and melting temperature T_m.

The moderate change of ΔG with temperature significantly below the melting temperature cannot explain the pronounced change in $u(T)$. Instead, the many orders of magnitude of change of crystallization speed (see both Equation (1) and

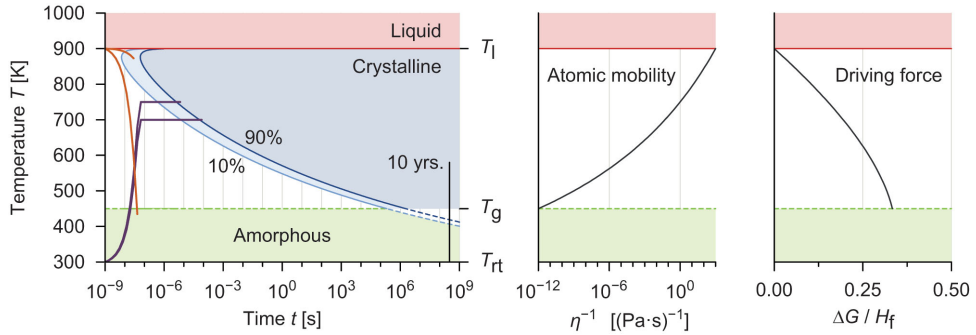

Figure 2. Temperature dependencies of crystallization kinetics (left), atomic mobility (middle) and driving force for crystallization (right). The atomic mobility is linked to the viscosity via the Stokes-Einstein equation in an inversely proportional way. For increasing temperatures the atomic mobility increases while the driving force for crystallization, the difference in Gibbs free energy ΔG between the liquid and crystal, decreases to zero at the liquidus temperature T_l (in this example at around 900 K). ΔG is plotted in units of the heat of fusion H_f. Although the driving force is large at low temperatures close to the glass transition temperature T_g, the atomic mobility is strongly reduced. Therefore, the regime of fast crystallization can be found at intermediate temperatures between T_l and T_g. Due to the interplay of the atomic mobility and the driving force, the crystallization does not occur immediately, when cooling a liquid below T_l. For rapid cooling rates of about 10^{10} K/s (orange line) the regime of fast crystallization can be bypassed and the material ends up in the melt-quenched amorphous phase. In case of much slower cooling rates, the phase-change material crystallizes. The blue curves indicate how much time it takes at a certain temperature to crystallize 10% and 90% of the volume respectively. While the amorphous phase-change material provides good data retention (over 10 years) at room temperature, the crystallization can take place on a nanosecond time scale at elevated temperatures (purple curves). Reproduced with permission.[24] Copyright 2011, Wiley-VCH.

Figure 2) originate mainly from the pronounced non-linearity in temperature dependence of atomic mobility $D(T)$, which is often expressed via the temperature dependence of viscosity $\eta(T)$ using the anti-proportionality of the Stokes-Einstein equation[37]:

$$D(T) \propto \frac{k_B T}{\eta(T)} \tag{3}$$

A breakdown of the Stokes-Einstein equation observed at temperatures close to T_g in various, especially fragile, supercooled liquids can be coped with a modification of the exponent $\xi \leq 1$:[96]

$$D(T) \propto \frac{k_B T}{\eta(T)^{\xi}} \tag{4}$$

This deviation has been commonly explained to originate from heterogeneous dynamics in supercooled liquids. In recent years, evidence from different experimental methods pointed towards the existence of extraordinarily high fragilities in phase change materials.[37,38] The according super-exponential deviation from a pure Arrhenius behavior in the temperature dependence of viscosity is traditionally described with the Vogel-Fulcher-Tamann equation:

$$\eta(T) = \eta_0 \exp\left(\frac{A}{T - T_0}\right) \tag{5}$$

with η_0, A and T_0 being constants.

With this high fragility of phase-change materials it is possible to explain the combination of a relatively wide window of fast crystallization at high temperatures with steeply increasing stability of the disordered phase towards lower/ambient temperatures, which is so beneficial for memory applications.

3.1.2. Nucleation

Without a preexisting crystal surface, the formation of a crystalline nucleus within the amorphous matrix is required, before the process of crystal growth can start.[24,27–29,32,33] In classical nucleation theory, the nucleation rate of crystallites in a non-crystalline surrounding is derived beginning with the driving force for the formation of a spherical crystalline cluster of atoms, that is, the difference in Gibbs free energy between the two phases:

$$\Delta G(r) = V(r) \cdot \Delta G_V + A(r)\sigma = \frac{4}{3}\pi r^3 \cdot \Delta G_V + 4\pi r^2 \sigma \tag{6}$$

Here, r is the radius, V the volume and A the surface of the nucleus, ΔG_V the difference in Gibbs free energy per unit volume and σ the interfacial energy per unit area. While the crystallization of a given volume leads to a reduction in total energy, the formation of a crystalline-to-amorphous interface costs energy. The critical radius r_C

$$r_C = \frac{2\sigma}{|\Delta G_V|} \tag{7}$$

describes the size of a crystalline cluster, at which the difference in Gibbs free energy (Equation (6)) reaches its maximum. For nuclei larger than that, i.e., $r > r_C$, a further crystal growth is energetically favorable, whereas for $r < r_C$ the free energy of the system is increased by adding further atoms to the subcritical cluster. Nevertheless, the latter process takes place due to thermally induced statistical fluctuations, which eventually lead to the formation of supercritical crystalline nuclei. The steady-state nucleation rate I_{SS}, that is, the number of supercritical nuclei forming per time and volume, is given by:

$$I_{SS} \propto \eta(T)^{-1} \exp\left(-\frac{\Delta G(r_C)}{k_B T}\right) = \eta(T)^{-1} \exp\left(-\frac{16\pi}{3k_B T}\frac{\sigma^3}{\Delta G_V^2} f(\theta)\right) \quad (8)$$

with $\eta(T)$ the temperature dependent viscosity. $f(\theta)$ accounts for the effect of heterogeneous nucleation at interfaces with the wetting angle θ.[97,98] For homogeneous nucleation this factor equals unity.

In general, both crystal growth and nucleation can be simultaneously present during crystallization. Which of these processes is dominating the crystallization process, strongly depends on the observed volume and the presence of preexisting crystalline surfaces in the surrounding. Because of the fact that nucleation rate and growth velocity have differing temperature dependencies, for example, maxima at different temperatures, the local device temperature can play an important role, too.[99]

An increase of the temperature in a phase-change memory element into the regime of fast crystallization needs sufficient Joule-heating and thus significant current densities. Since the resistivity of the amorphous phase is high and the available voltages in a memory device are typically limited to a few volts, the increase in local temperature could, in principal, pose a challenge to the ability to electrical switch a phase-change memory element. Thus, the existence of a pronounced non-linearity in the current–voltage characteristic of these amorphous materials is essential for a memory application. Especially the quite abrupt transition from a poorly to a highly conductive amorphous state at high electrical fields (threshold switching) is an enabling feature.

3.2. Threshold Switching

Since the discovery of the threshold-switching effect in 1968 by Ovshinsky[100] several different physical mechanisms have been proposed for its explanation. An extensive discussion about whether the driving force for this reversible switching phenomenon is controlled by a thermal or by an electronic effect was settled in the 1980s in favor of an electronic excitation mechanism.[101–104] While today there is a broad agreement about the electrical-field-driven nature of the reversible threshold-switching,[39,105–107] thermal effects are also considered, especially when dealing with nano-scale devices. In order to give an impression of the current discourse on the potential mechanisms behind threshold switching, three incompatible models are highlighted.

Ielmini et al. proposed a widely cited model for the sub-threshold conduction and the transient effect of threshold switching in amorphous phase-change materials. In their work, the non-linear current–voltage characteristic at moderate fields is explained by the Poole-Frenkel effect. Here, the potential energy barrier for excitation of trapped charge carriers into conducting states is reduced by the presence of near trap states and by the electrical field, which thereby strongly enhances the electrical conductivity. In 2007, Ielmini et al. extended this existing model for the steady-state transport in amorphous solids[108–110] in order to also explain the regime at high electrical fields where threshold switching occurs.[39] Under the influence of strong fields charge carriers can be excited from deep trap states into shallow trap states close to the band edge. A relaxation mechanism counteracts the carrier generation leading towards a steady-state distribution. When enough carriers are excited into shallow trap states, threshold switching occurs.

The second model, which should be highlighted was first proposed by Adler et al. in 1980[111] and more recently reformulated by Pirovano et al. and Redaelli et al.[105,106] Similar to Ielmini´s model, the threshold switching effect is described by an interaction of charge carrier generation and recombination mechanisms, whereas the electrical conduction is explained by trap-limited band transport. In case of low electrical fields, most of the generated free charge carriers can recombine via Shockley-Hall-Reed and/or Auger recombination. The generation mechanism (e.g., impact ionization and avalanche multiplication) strongly depends on the electrical field and the concentration of free carriers. In this model the breakdown in conductivity occurs at large electrical fields, when all traps close to the band edge are filled and the rate of recombination saturates. In this moment the process of recombination cannot counter-balance the generation of charge carriers anymore, leading to a strong increase in free charge carriers in the conduction band and thereby to threshold switching. Although both mechanisms for threshold switching proposed by Ielmini et al. and by Pirovano et al. appear to be similar on the first view, it has to be noted that the generation and recombination mechanisms as well as the detailed dependencies on the electrical field and charge carrier concentration differ significantly.

Thirdly, as an extension to the classical nucleation theory, Karpov et al. proposed a field-induced nucleation model to explain the threshold-switching phenomenon.[107,112] In this model, the electrostatic energy and thereby the free energy of a system is reduced by the formation of a crystalline nucleus within the amorphous material under bias. The energy barrier for the formation of a stable nucleus as well as the critical radius is reduced in the presence of an electrical field, which facilitates the nucleation process (see **Figure 3**a). According to Karpov et al. the nucleation takes place heterogeneously at the interface between electrode and phase-change material.[112] Once a crystalline nucleus is formed, it grows into a cylindrical filament. It thereby enhances the electrical field in the amorphous material at the tip of the filament accelerating further nucleation in this region. In the moment when the crystalline filament fully bridges the two electrodes, the threshold-switching becomes observable as a pronounced increase in conductance of the memory device.

If the electrical field is removed before the crystallite has grown larger than the critical radius for the field-free case, the conductive filament decays. This way the field-induced reduction in the critical radius can explain the transient nature of the threshold switching event and the relaxation from the highly conductive amorphous "ON-state" back to the poorly conductive amorphous "OFF-state".

3.3. Ion Migration

In the physical processes considered for crystallization and threshold switching atoms need to change their positions

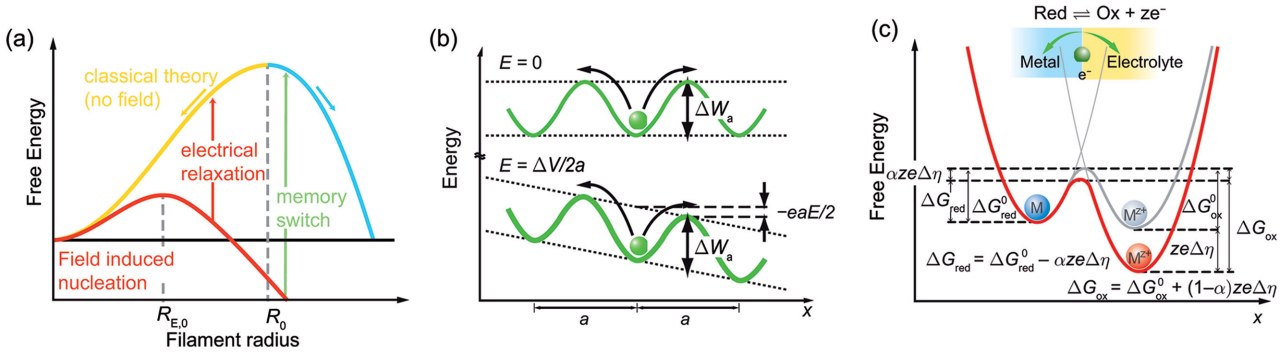

Figure 3. a) Free energy of a crystalline nucleus or filament as a function of its size. In comparison to the field free situation (yellow and blue curves), under the influence of an electrical field (red curve) both the critical radius and the according free energy that needs to be overcome for the formation of a stable crystalline nucleus are reduced. This way the electrical field facilitates the creation of a crystalline nucleus. When the radius of a nucleus has grown between $R_{E,0}$ and R_0, it is stable under the presence of the electrical field, but not when its absent. In case of a reduction of the electrical field to zero, the free energy is minimized by a shrinkage and subsequent decay of the nucleus. In contrast, nuclei that had enough time to grow larger than R_0 under electrical bias are even stable in the field-free situation. b) Schematic presentation of a random jump of an ion overcoming a potential barrier ΔW_a. upper figure: without externally applied electric field E; lower figure: electric potential gradient $E = \Delta V/2a$ showing that the potential barrier to the right is reduced by $W = eaE/2$. c) Illustration of the energy profile of an electron transfer reaction at the interfaces between a metal atom M at the surface of the metal electrode and a corresponding cation M^{z+} within the outermost layer of the electrolyte as described by the Butler-Volmer equation. The grey line represents the equilibrium situation, and the red line represents the situation with an overpotential applied. (b,c) are are reproduced with permission.[81] Copyright 2012, Wiley-VCH.

only very moderately, that is, with respect to their direct neighbors, if at all. Quite contrary, ions when exposed to an electric field can move over much longer distances. Ions move by hopping from site to site over a barrier ΔW_{hop} in the resistive switching layer. The average distance between these sites is called hopping distance a and it is typically in the order of interatomic distance, that is, 0.2–0.5 nm. Without applied electric field this motion occurs randomly due to thermal fluctuations with a net motion only in case of a concentration gradient. By application of an electric field E the ion movement becomes directional. If an electric field is applied, the hopping barrier is affected according to $\Delta W_{hop} = \Delta W_{hop,0} \pm 1/2zeaE$ (cf. Figure 3b). This leads to a hyperbolic sine term in the mathematical description of the ionic hopping current density

$$j_{hop} = 2zecaf \exp\left(-\frac{\Delta W_{hop,0}}{k_B T}\right)\sinh\left(\frac{aze}{2k_B T}E\right) \quad (9)$$

Here, z is the charge number, e the elementary charge, c the ion concentration, and f the attempt frequency. Equation (9) is also called the Mott–Gurney law for ion hopping. For low electric fields the ionic current density depends linearly on the electric field, whereas for high electric fields the dependence becomes exponential. The electric field that drives the ion motion is the average electric field resulting from the voltage V that drops over a certain distance w, that is, $E = V/w$. In literature some groups used the local Lorentz field in order to calculate the ion-hopping-current,[113–115] which results in a stronger nonlinearity. This proposition, however, is incorrect as the electric field experienced by the moving ion spatially fluctuates and the Lorentz field gives only the maximum value as pointed out by Meuffels et al.[116] Thus, the use of the average field is indeed the correct approach.

3.4. Electron-Transfer

A further rate-limiting step can be attributed to redox reactions occurring at the metal/insulator interfaces, for instance, the oxidation of an oxidizable electrode. The energy diagram of this process is shown in Figure 3c. The left potential well describes the potential energy of a metal atom M at the metal surface, whereas the right one is attributed to the corresponding metal ion M^{z+} close to the metal surface. ΔG_{ox} and ΔG_{red} denote the activation energies to oxidize a surface metal atom and to reduce a M^{z+} ion, respectively. Without an external electrical field, the oxidation current density j_{ox} and the reduction current density j_{red} correspond to the exchange current density $j_{0,et} = j_{ox} = |j_{red}|$ and thus there is no net current flow. Taking into account the reaction rate constants k_{ox} and k_{red}, the current densities are given by:

$$j_{ox} = zeck_{ox}\exp\left(-\frac{\Delta G_{ox}}{k_B T}\right) \text{ and}$$
$$j_{red} = zeck_{red}\exp\left(-\frac{\Delta G_{red}}{k_B T}\right) \quad (10)$$

By application of a negative potential to the metal electrode its Fermi energy is increased by $-ze\Delta\varphi_{et}$, where $\Delta\varphi_{et}$ represents the additional voltage (or overpotential) drop across the interface. Consequently, the activation energies are altered and in the case of Figure 3c the reduction process is favored over the oxidation process. The change of the activation energy is proportional to the overpotential, whereas the charge transfer coefficient α determines how the individual activation barriers are lowered. The values of the charge transfer coefficient lie between 0 and 1. The net current density across such an interface j_{et} due to the involved charge transfer, can be described by the Butler-Volmer equation

$$j_{et} = j_{0,et}\left[\exp\left(\frac{(1-\alpha)ze}{k_BT}\Delta\varphi_{et}\right) - \exp\left(-\frac{\alpha ze}{k_BT}\Delta\varphi_{et}\right)\right] \quad (11)$$

If $\Delta\varphi_{et} > 0$ the oxidation reaction dominates, that is, described by the left term in Equation (10). In contrast, the reduction reaction prevails if $\Delta\varphi_{et} < 0$.

3.5. Electrocrystallization

Electrocrystallization denotes nucleation and crystal growth in electrochemical systems under influence of the electric field.[117,118] In contrast to the crystallization discussed in Section 3.1, during electrocrystallization also a charge transfer is involved, for example, in the process of nucleation of Ag/Cu on the inert electrode prior to filamentary growth in an ECM cell. To be stable the nucleus must have a critical size/radius, which is related to a critical number of atoms N_c. By application of an overpotential $\Delta\varphi_{nuc}$ this critical nucleus size is reduced, as is the nucleation barrier ΔG_{nuc} (cf. Figure 3a). The nucleation time, which is the required time to form a stable nucleus, can be calculated according to[118,119]

$$t_{nuc} \propto \exp\left(\frac{\Delta G_{nuc}}{k_BT}\right)\exp\left(-\frac{(N_c+\alpha)ze}{k_BT}\right)\Delta\varphi_{nuc} \quad (12)$$

where α is again the charge transfer coefficient. The critical number of atoms can be any integer number including zero.[117,120] In the latter case every reduced atom can be regarded as a stable nucleus. In contrast for $N_C = 1$, the reduced atom needs to find a stable surface site in order to act as a stable nucleus. After nucleation a metal phase can grow. According to Faraday, the growth rate v_{growth} is directly proportional to the ionic current J_{ion}:

$$v_{growth} = -\frac{M_{Me}}{ze\rho_{m,me}}J_{ion} \quad (13)$$

Here, M_{Me} denotes the atomic mass of the deposited metal, and $\rho_{m,me}$ its mass density.

3.6. Analysis of the Intrinsic Non-Linearity for Redox-Based Resistive Switching Processes

In a particular VCM/ECM cell all of the processes described in Sections 3.3, 3.4 and 3.5 might be present. The slowest one, however, will limit the switching speed. It is not straightforward to identify the limiting process from a switching-time (t_{sw})–switching-voltage (V_{sw}) diagram. Despite their different physical and electrochemical nature all of these field-induced processes are related to an activation barrier and thus obey an Arrhenius-type law. Hence, all processes can be exponentially enhanced when the local temperature increases due to local Joule heating. In addition, the activation barrier can be lowered by an applied electric field/voltage resulting in an exponential dependence on the voltage, at least when the electric field is high enough. Thus, the different processes result in different slopes in a $\ln(t_{sw})$ – V_{sw} diagram due to the physical parameters involved if only a single process is considered. In a pulse experiment the slope is related to the coefficients in the exponential term of the rate-limiting equation. According to Equation (9)–(12), the slopes

$$m_{hop} = -\frac{aze}{2k_BTw}, m_{red} = -\frac{aze}{k_BT}, m_{ox} = -\frac{(1-\alpha)ze}{k_BT}, \text{and } m_{nuc} = -\frac{(N_c+\alpha)ze}{k_BT} \quad (14)$$

can be extracted for the ion hopping, reduction, oxidation and nucleation process, respectively. The slopes for the reduction and oxidation reaction are only valid if only one of the reactions is considered. In fact always both reactions will take place, which would lower the slope. Instead of using the slope m for comparison of the different processes, it is more straightforward to calculate the voltage increment ΔV_{10x} that is required to accelerate the switching process by a factor of 10 in time. This voltage increment can be given by

$$\Delta V_{10x} = -\frac{1}{m}\ln(10) \quad (15)$$

In experiment the voltage increment ΔV_{10x} can be extracted. Using Equation (14) and (15) the required physical parameters assuming a single limiting process can be calculated and checked for physical meaningfulness. Here, two cases are of special interest: i) If the product of the experimentally determined slope $|m|$ and k_BT/ze is larger than 1, that is, $|mk_BT/ze| > 1$, then nucleation can be identified as the limiting process, because all other processes cannot accomplish such a steep slope with physically reasonable parameters. ii) For the ion hopping processes, a physically reasonable value for the ratio a/w should be smaller than 1/5. This means with a reasonable hopping distance of 0.3–0.5 nm the voltage is assumed to drop over a distance of not less than w = 1.5–2.5 nm. Note that this distance w is still very small. As a consequence, if the experimentally determined normalized slope $|mk_BT/ze|$ is found to be larger than 1/5, ion hopping can be excluded as the only limiting process.

To compare the non-linearity of these processes the corresponding slopes are plotted as normalized switching time versus applied voltage in **Figure 4** for some limiting cases, which are described in the figure caption. Based on these limiting cases (for z = 2) the voltage increments necessary to cause a change in switching time by one decade can be determined to 397 mV/dec < $\Delta V_{10x,hop}$ < 4.97 V/dec for ion hopping, 33 mV/dec < $\Delta V_{10x,et}$ < 298 mV/dec for electron-transfer, and 8 mV/dec < $\Delta V_{10x,nuc}$ < 27 mV/dec for nucleation limiting the switching kinetics, respectively. Note that the calculated values have to be doubled for z = 1. Thus, the highest non-linearity would be achieved by nucleation followed by electron-transfer and ion hopping. When more then a single process is present in a specific device, the slowest process will determine the slope in the t-V diagram in a certain voltage regime. The slope for nucleation is so steep that it is very likely that this process limits the switching speed only at small voltages. In contrast, a process with a flat slope limits the switching process very likely at higher voltages. Thus, it is expected that the slopes of the total

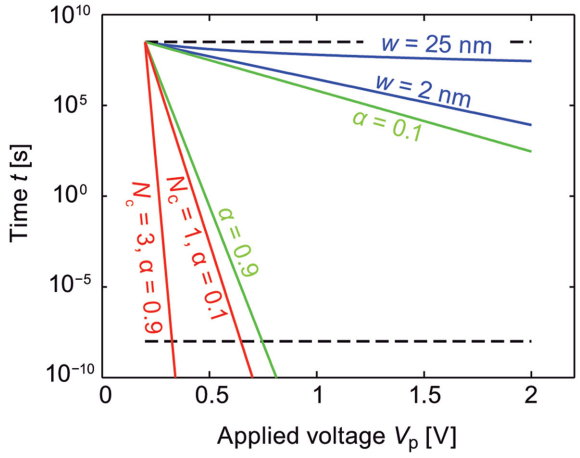

Figure 4. Illustration of the non-linearity in the switching kinetics obtained for electric field enhanced nucleation (red), electron transfer reaction (green), and ion migration (blue) in the limiting scenarios explained below. The different processes cover a different range of slopes in the t–V diagram. For the ion migration curves $a = 0.3$ nm and $w = 2$ nm and 25 nm are chosen as lower and upper limit. The charge transfer coefficient is chosen in a range between $0.1 \leq \alpha \leq 0.9$ and for the nucleation $N_c = 1$, $\alpha = 0.1$ and $N_c = 3$, $\alpha = 0.9$ are used. For all lines $z = 2$ is assumed.

switching process become flatter with increasing voltage. This is true as long as only voltage/field acceleration is involved. In the previous estimations it has been assumed that it is always the total applied voltage that accelerates the switching speed. In a real device, however, part of the voltage can drop over series resistances. Thus, the slope in the t_{sw}–V diagram should actually be flatter than how it appears when using the total voltage.

The discussion of the slopes does not consider the limit of the acceleration. Each physical process, however, is related to a certain barrier height. The field/voltage acceleration in Equation (9)–(12) results from a barrier lowering effect. Accordingly, the mathematical description of thermally activated processes is only valid as long as the effective barrier ΔW_{eff} is still larger than zero. Consequently, the given switching time estimations are only valid up to a certain maximum voltage V_{max} which can be given by $V_{max} = \Delta W/(k_B T m)$. The activation energy of the specific processes indicates how many orders of magnitude in non-linearity can be achieved. Higher activation energies correspond to a stronger non-linearity. For memory applications more than 15 orders of magnitude in time must be spanned. Thus, in the framework of field-induced barrier lowering the unaltered activation energy has to be higher than $\Delta W_{min} \geq k_B T_0 \cdot \ln(10^{15}) = 0.89$ eV at an operation temperature $T_0 = 300$ K in order to provide enough room for barrier lowering by applying voltages.

Besides the electric field also temperature can accelerate the switching process as expressed by the Arrhenius-type of the above equations. Here, we will exemplarily discuss the temperature acceleration of the ion hopping process. The conclusions, however, can be also extended to the other processes. If we consider a filamentary switching mechanism, local Joule heating can occur due to the high current densities. The temperature increase in a cylindrical filament can be approximated by

$$T = T_0 + R_{th} P_{el} \tag{16}$$

where T_0 is the ambient temperature and P_{el} the electrical power dissipated in the VCM cell. The thermal resistance R_{th} depends on the thermal and electrical conductivity of the filament, which are parameter of the filament material, as well as its geometry, for example, R_{th} becomes larger for smaller filament diameter and thus higher temperature result.[121] For a conical shaped filament, the hottest spot is expected to appear close to the thinnest part.[60,122] The environment (surrounding materials) and the cell geometry influence the thermal resistance, too. To enable efficient heating a bad heat dissipation via the electrodes and the surrounding insulating material is advantageous. This means materials with a low thermal conductivity are beneficial in this respect.[123,124] To illustrate the interdependence of non-linearity and dissipated electrical power, we use two different current–voltage scenarios: an Ohmic and a diode like behavior, as illustrated in **Figure 5**. The corresponding parameters are given in the

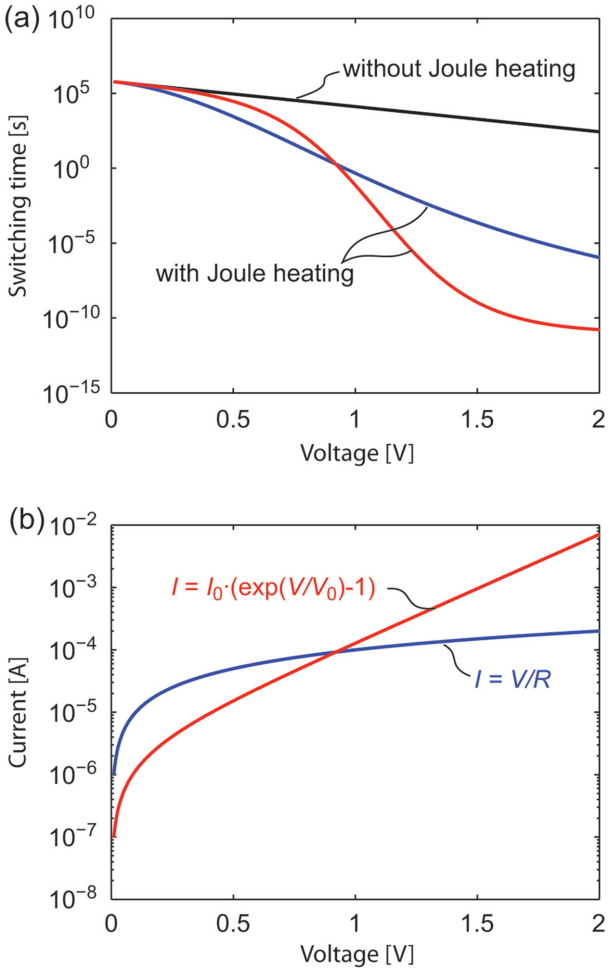

Figure 5. a) Illustration of the switching time vs applied voltage calculated without Joule heating (black solid line) and with Joule heating assuming a linear I–V relation (blue solid line) and a diode like I–V behavior (red solid line). The corresponding I–V characteristics are shown in (b) using the same color code. The parameters used are: $a = 0.5$ nm, $\Delta W_{hop} = 1$ eV, $V_0 = 0.25$ V, $I_0 = 2.38$ μA, $R = 10$ kΩ, $R_{th} = 1.25 \times 10^6$ K/W.

figure caption. The local Joule heating effect clearly increases the switching speed. For the diode-like *I–V* behavior, at low voltages the current is too small to induce Joule heating and thus the corresponding *t–V* behavior (red solid line) equals the constant temperature case shown as solid black line. Then Joule heating sets in and the slope becomes steeper than in the case of sole voltage/field acceleration. By comparing the two current–voltage scenarios it appears that the non-linearity is highly dependent on the non-linearity of the *I–V* relation as the Joule heating is power-dependent. In fact, the non-linear switching kinetics in the Joule heating regime become power-dependent rather than field-dependent as shown for TaO_x-based VCM cells.[125] At high voltages the slope flattens again, as the slopes are in fact decreasing with temperature and additional Joule heating does not result in a large acceleration (cf. Equation (14)).

It depends on the particular ReRAM cell whether field or temperature acceleration dominates. Furthermore, the ratio between field or temperature acceleration also depends on the considered voltage regime. For low voltages the dissipated power might be so low that no Joule heating at all occurs and thus only field acceleration is present. At higher voltages Joule heating might set in additionally accelerating the switching process. Independent of temperature and field acceleration, the activation energy for the limiting processes must be sufficiently high to allow fast switching and robust retention as discussed for the field acceleration. This gives a design path for material selection and engineering.

4. Experimental Observations in Resistive Memory Device

In order to show that the voltage-time dilemma can be overcome for a particular type of memory device, it needs to be proven that the SET and RESET operations are as fast as 10 ns and the cells show a read-disturb immunity up to 10 years. For the latter condition the determining operation (SET or RESET) needs to be identified. In phase-change materials the crystalline phase is the thermodynamically stable one, whereas the amorphous phase is metastable. Thus, the stability of the HRS state during read-out should be considered. As VCM and ECM devices exhibit a bipolar operation, it depends on the chosen read voltage polarity whether the read-out stability of the HRS or LRS state needs to be investigated. As data on RESET kinetics are rare, we will focus the discussion on the SET process and thus the read-out stability of the HRS.

4.1. Electrochemical Metallization Memories

The switching kinetics of a various ECM cells have been studied using different measurement methods. Due to the relevance for device operation, mainly SET pulse studies of switching kinetics appear in literature, while SET sweep mode analyses and RESET investigations are rare.[48,126,127] In **Figure 6** the published data of SET switching times t_{sw} at room temperature as function of the pulse voltage V_p are compiled.[42,43,46,47,66–68,128,129]

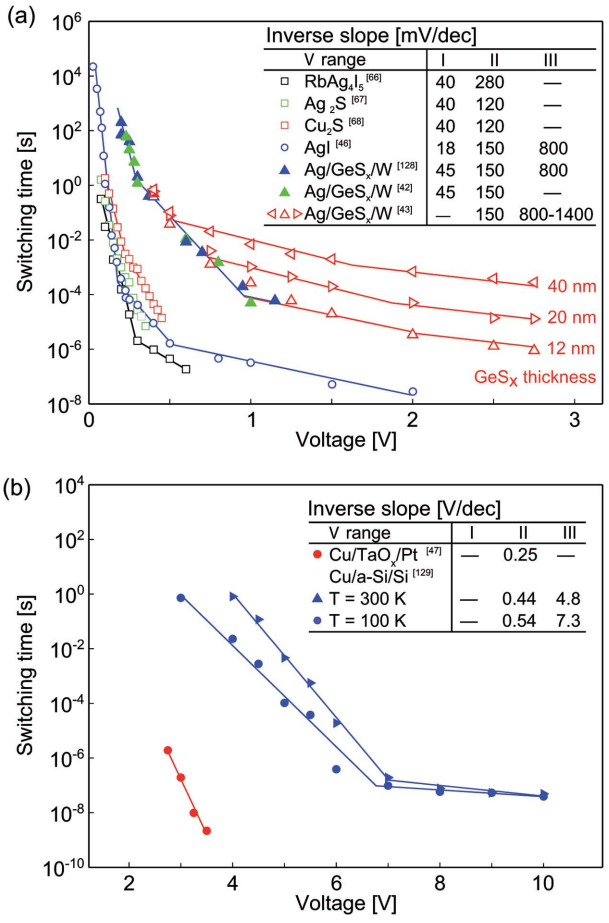

Figure 6. Switching kinetics log *t–V* of ECM cells showing different inverse slopes in the specific voltage regimes "low" (I), "medium" (II). "high" (III) for: a) primary solid electrolytes Ag_2S,[66] Cu_2S,[67] $RbAg_4I_5$,[68] and AgI[46] as well as secondary solid electrolytes Ag-GeSx,[42,43,128] and b) untypical solid electrolytes Cu/TaOx/Pt[47] and Cu/a-Si/Si.[129]

Three different groups of data sets with similar switching kinetics can be identified. It makes sense to introduce a new classification in the following way: i) primary solid electrolytes like Cu_2S, Ag_2S, AgI or $RbAg_4I_5$ where the metal species of the composition are intrinsically present as cations, ii) secondary solid electrolytes like GeS_x or $GeSe_x$ which are well-known ionic conductors for Ag or Cu cations which are extrinsically delivered by doping during processing and/or by diffusion from the electrode (e.g., in an $Ag/GeS_x/W$ stack) after deposition, and iii) untypical solid electrolytes like a-Si and Ta_2O_5 which differ from the latter type because the necessary counter charge is provided by ionic injection into the material. For Cu/Ta_2O_5 and Cu/SiO_2 systems it has been shown that the counter charges are possibly OH^- ions provided by residual water within the thin film.[130–132] Thus, water serves as electrolyte and the solubility of Cu/Ag ions depends on the amount of water remaining in the system.

In the framework of this classification the gap-type atomic switches as $Pt/air\text{-}gap/RbAg_4I_5$,[66] $Pt/air\text{-}gap/Ag_2S$,[67] and $Pt/air\text{-}gap/Cu_2S$,[68] are attributed to primary solid electrolytes even if the filament is not growing in the electrolyte but in the gap.

A very general analysis of Figure 6 may end in the statement that the switching voltage is possibly related to the cation concentration. In primary solid electrolytes this concentration is very high and the switching takes place at very low voltages. Untypical solid electrolytes with probably the lowest ion concentrations switch at the highest values. Furthermore, on the one hand primary and secondary solid electrolytes tend to higher ion mobilities, and on the other hand ion mobility is dependent on concentration as demonstrated for example for Cu/Ag ions in SiO_2 system.[63]

It should be mentioned at this point that in case of ECM cells the HRS resistances are very high and Ag and Cu are very good heat conductors. Therefore, a temperature – acceleration of the SET kinetics can be neglected, and we will only consider field/voltage acceleration of the involved physical processes in the following discussion. The essential fact represented in the t_{sw}–V_p diagram of Figure 6 is the occurrence of more than one slope indicating the existence of different physical processes as nucleation, electron – transfer, or ion hopping limiting the switching speed. As expected from the discussion in Section 3.6 the steepest slope arises for the lowest voltages. For increasing voltages the slope becomes flatter.

The systems Cu_2S, Ag_2S, and $RbAg_4I_5$ counting to the primary solid electrolytes show a very steep slope in the beginning, requiring only about 40 mV for a change of switching time by one decade. The charge state of a Ag ion is always $z = +1$ and the charge state of Cu in the Cu_2S is also + 1 due to its bond nature. Thus, this slope can only be explained by a nucleation limitation as the $|mk_BT/ze| = 1.48 > 1$, which results in a critical nucleus size of $N_C = 1$ and $\alpha = 0.48$ (compare Equations (14) and (15)). At higher voltages a second more shallow slope between 120 to 280 mV/dec is observed, which fits in a limitation either by nucleation with $N_C = 0$, or by ion transport to the tip as it has been proposed for the Cu_2S system.[68] The authors of that study extracted from temperature-dependent measurements a single activation energy $\Delta W_a = 1.38 \pm 0.16$ eV for all applied voltages. This suggests that either a nucleation process with two different critical nuclei or two different processes with similar activation energies are responsible for the limitation at voltages under test. In Ag_2S atomic switches, two different slopes in the t_{sw}–V diagram at different voltage regimes are observed, too.[67] However, the different voltage regimes are linked with different activation energies ($\Delta W_a = 0.58$ eV at lower voltages and $\Delta W_a = 1.32$ eV at higher voltages) which is a clear indication that two physical processes occur.

From temperature-dependent measurements of $RbAg_4I_5$ atomic switches an activation energy of $\Delta W_a = 1 \pm 0.1$ eV has been determined,[66] which is much higher than the diffusion barrier of Ag ions within $RbAg_4I_5$ $\Delta W_a = 0.16$ eV.[133] Therefore, ion transport can be excluded to be rate-limiting. Thus, the second slope in the t_{sw}–V diagram is related with a nucleation or an electron-transfer process.

The Ag/AgI/Pt cell exhibits three different slopes, which indicates that at least three different processes are limiting the switching speed. At low voltages below 0.3 V a slope of 18 mV/dec appears. Thus, a nucleation limited process with $N_C = 3$ and $\alpha = 0.3$ is anticipated. For higher voltages the slope degrades to 150 mV/dec and further to 800 mV/dec. Hence, electron-transfer and ion hopping processes could be responsible for determining the switching kinetics.

The switching kinetics data of the different Ag/GeS_x/W ECM cells (secondary solid electrolytes) shown in Figure 6 converge to a single slope of ≈45 mV/dec for voltages lower than 0.5 V corresponding to a nucleation limitation with $N_C = 1$ and $\alpha = 0.32$. For higher voltages two additional slopes emerge, which could be possibly attributed to a combination of electron – transfer and/or ion hopping limitation as in the case of the Ag/AgI/Pt cell. The different data of the Ag/GeS_x/W ECM cells originate from diverse sources and mainly differ in the thickness of the electrolyte. The spreading of the data at higher voltages may be attributed to the length of the growing filament and suggest that electron-transfer and/or ion migration play the decisive role for limiting the switching speed. In addition, the concentration of Ag ions dissolved into the GeS_x thin film might depend on its thickness. Jameson et al. also measured the temperature dependence of the Ag/GeS_x/W switching kinetics and could extract an activation energy of 0.48 eV for voltages higher than 1 V.[43] Similar values were reported by Russo et al.[128] (0.5 eV) and Palma et al. (0.4 eV).[42] The coincidence of all the curves in the low voltage regime, i. e. no thickness dependence, is characteristic for the nucleation limitation.

The Cu/TaO_x/Pt device, a representative of the untypical solid electrolyte, exhibits only a single slope of ≈240 mV/dec (cf. Figure 6) if data only of a very small voltage range are discussed. The analysis presented in Section 3.6 is successful for the following parameters: ion hopping distance $a \approx 4.2$ nm, critical nucleus $N_C = 0$ and charge transfer coefficient $\alpha = 0.24$ (for $z = +2$) or 0.12 (for $z = +1$). In this scenario every reduced copper atom can serve as nucleus for filamentary growth. Since a hopping distance of several nm makes no physical sense, switching limited by electron-transfer reactions and/or nucleation processes might be responsible for the observed kinetic data.

The Cu/a-Si/Si switching kinetics data in Figure 6 show a very remarkable feature. At voltages below 7 V two different slopes of about ≈570 mV/dec and ≈800 mV/dec can be extracted for $T = 300$ K and $T = 100$ K, respectively. In contrast, these slopes converge to a single one at higher voltages. As the devices are 2.5 µm in diameter[129] the second slope could also be caused by the RC–time of the device under test and is not necessarily a footprint of a second process limiting the switching process. The two extracted slopes are quite shallow, thus it is very likely that the filamentary growth is limiting the switching speed rather than the formation of a nucleus. The temperature increase from 100 K to 300 K show an acceleration of the switching speed, however, the slope of the 300 K-curve is not simply one third of that of 100 K as it is expected from Arrhenius-type behavior of the underlying physical processes discussed in Section 3.6.

To evaluate the contribution of each individual process to the switching kinetics data of the Ag/AgI/Pt cell Menzel et al. developed a one-dimensional simulation model for the simulation of ECM cells that include nucleation, electron-transfer reactions, ion hopping transport and filamentary growth,[46,53] which has been subsequently extended to include the switching variability.[134] In this model a cylindrical filament is considered that grows/dissolves during resistive switching (cf. **Figure 7**a).

The resistance change is attributed to the modulation of a tunneling gap x between the filament tip and the active

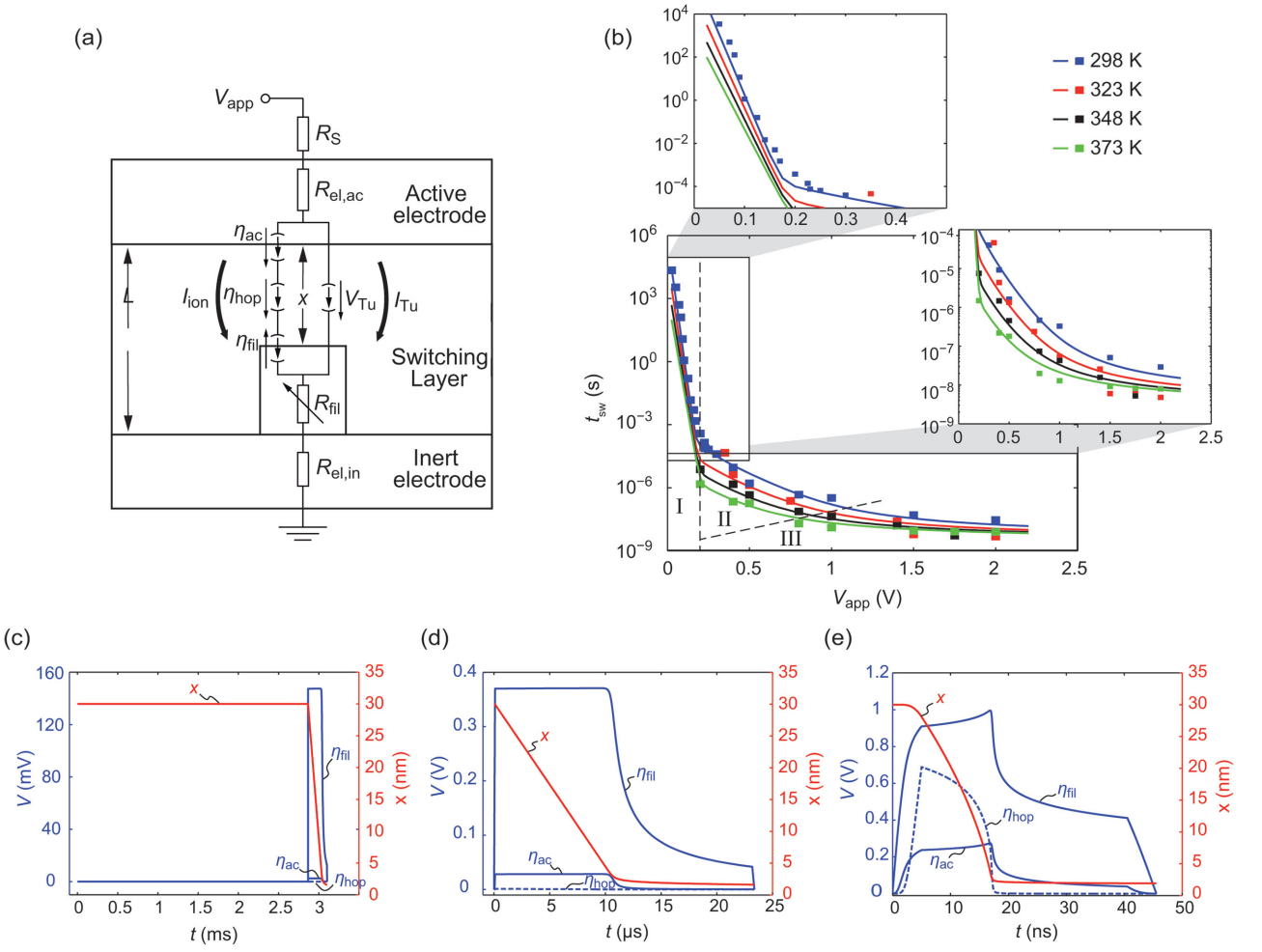

Figure 7. a) Schematic of the ECM switching model with an equivalent circuit diagram. A switching layer of thickness L is sandwiched between the active top electrode and the inert bottom electrode. A cylindrical filament grows within switching layer and modulates the tunneling gap x between the filament and the active electrode. In the switching layer both ionic and electronic current paths are present, respectively. b) Pulsed SET switching kinetics of a AgI-based ECM cell for different ambient temperatures $T = 298$ K (blue), 323 K (red), 348 K (black), and 373 K (light green). The simulated data are displayed using solid lines and the experimental data using squares. I, II, III mark the nucleation limited, the electron transfer limited and the mixed control regime, respectively. The corresponding transient overpotentials (blue) and tunneling gaps (red) are shown for an applied voltage of c) 0.15 V representing the nucleation limited regime, d) 0.4 V representing the electron transfer limited regime and e) 2V, which corresponds to the mixed control regime. In (c,d) the hopping overpotential is illustrated with blue dashed lines and the electron transfer overpotentials with blue solid lines. Reproduced with permission of the PCCP Owner Societies.[46] Copyright 2013, Royal Society of Chemistry.

electrode. The growth/dissolution of the filament and thus the change of the tunneling gap is modeled using Faraday's law (cf. Equation (13))

$$\frac{dx}{dt} = -\frac{M_{Me}}{ze\rho_{m,me}} J_{ion} \tag{17}$$

and is driven by the ionic current density J_{ion}. In Equation (17) M_{Me} denotes the atomic mass of the deposited metal, and $\rho_{m,me}$ its mass density. The ionic current can be calculated using the equivalent circuit diagram in Figure 7a. Here, the voltage controlled current sources $\Delta\varphi_{fil}$, and $\Delta\varphi_{ac}$, represent the charge transfer overpotentials at the filament/insulator and active electrode/insulator interface, respectively. The corresponding ionic current is calculated according to the Butler-Volmer equation. $\Delta\varphi_{hop}$ represents the overpotential resulting from the ion hopping transport, which is modeled according to the Mott-Gurney law for ion hopping (9). The electronic current I_{Tu} in this model is calculated using Simmons equation for electron tunneling at intermediate voltages[46,53] and it depends on the tunneling gap x. The remaining elements of the equivalent circuit diagram are the filament resistance R_{fil}, which depends on x, the resistances of the active electrode $R_{el,ac}$ and the inert electrode $R_{el,in}$ as well as an optional serial resistor R_S. To include the nucleation process, the nucleation time is calculated according to Equation (12) and then the filamentary growth is simulated by solving the differential Equation (17). Using this simulation model, Menzel et al. could reproduce the experimental switching kinetics data of Ag/AgI/Pt devices over 12 orders of magnitude at different ambient temperature.[46]

The corresponding simulation data is shown as solid lines in Figure 7b, whereas the experimental data is depicted as squares. By analyzing the tunneling gap and voltage transients three different regimes could be identified. For very low voltages V_{app} < 0.2 V the switching time is given by the time to form a stable nucleus. For example at 0.15 V the nucleation time is t_{nuc} = 2.8 ms accounting for most of the switching time as illustrated in Figure 7c. During the nucleation the electron transfer overpotentials $\Delta\varphi_{fil}$, $\Delta\varphi_{ac}$ as well as the hopping overpotential $\Delta\varphi_{hop}$ are zero. Accordingly, the filament does not grow and the tunneling gap remains constant. After nucleation the filament grows comparatively fast until the current compliance is reached. In contrast, no nucleation regime is visible in regime II as illustrated in Figure 7d for an applied voltage of 0.4 V. The filament immediately starts to grow and the voltage is divided between the overpotentials $\Delta\varphi_{fil}$ and $\Delta\varphi_{ac}$. As the hopping overpotential is zero, the switching kinetics are limited by the electron transfer reaction. In regime III also a significant hopping overpotential emerges in addition to the electron transfer overpotentials (cf. Figure 7e). Thus, this regime is controlled by both processes electron-transfer and ion hopping and it is consequently called mixed control regime. Based on the temperature-dependent data different activation energies have been extracted for the nucleation, electron-transfer and ion hopping processes, that is, 0.8, 0.6, and 0.32 eV, respectively.[46] The latter value has been confirmed by Tappertzhofen et al. performing independent measurements.[135]

The collected SET pulse switching data in Figure 6 show that a very high non-linearity of the switching kinetics is achieved in ECM devices. However, often only a small voltage regime is investigated and thus a full understanding of the cell switching kinetics is lacking in these cases. In addition, the question remains whether long retention and fast switching can be achieved in these systems. Recently, Calderoni et al. demonstrated on a test array that their ECM device can switch between HRS and LRS up to 10^6 times using 300 ns pulses.[136] In addition, a very promising bit error rate results after a 1hr bake at 150°C. An extrapolation of this experiment with an activation energy of 1.5 eV yields a retention of 10y. In addition, Belmonte et al. demonstrated up to 10^6 switching cycles using 10 ns pulses in integrated 90 nm W/Al_2O_3/TiW/Cu 1T1R ECM cells.[126] The same cells showed a high read-disturb immunity at a constant voltage stress of ±0.5 V for the HRS/LRS at room temperature and 125°C. The extrapolation of the pulse-programming data of these cells for SET and RESET predict that the LRS and HRS are stable over 10 years at ±0.5 V. In this stack the TiW layer was included to prevent an easy injection of Cu, effectively increasing the injection barrier, into the Al_2O_3 oxides and a device failure. This "barrier design" has been also achieved by inserting a thin Ti layer into a W/Al_2O_3/Ti/CuTe/Pt stack.[137] Guy et al. showed that non-linearity of the switching kinetics of Al_2O_3-based ECM cells can be improved by reducing the switching layer thickness.[138] Moreover, they could optimize the RESET efficiency of a MO_x-based ECM cell can be improved by inserting a thin HfO_2 layer at the inert electrode.

The latter examples demonstrate that the voltage–time dilemma can be solved in electrochemical metallization memories by cell design.

4.2. Valence Change Memories

The SET and RESET switching kinetics for VCM devices has been investigated for different device stacks. As in the case of ECM devices we will focus our discussion on the SET kinetics that is obtained by pulse measurement. In this case the SET time can be clearly identified by an abrupt increase of the current in the current transient. In contrast the RESET operation in VCM cells is rather gradual. Thus, the RESET time also depends on its definition in the individual studies, which prevents to make a fair comparison. The published switching kinetics data of TiN/HfO_x/TiN,[76,139] TiN/HfO_x/AlO_x/Pt,[140] Ti/HfO_x/Pt,[141] Pt/TiO_x/Pt,[142] Pt/TaO_x/Ta,[125] and Pt/$SrTiO_3$/Ti[143] devices using pulse experiments are illustrated in **Figure 8**. In contrast to the ECM switching kinetics data, the observed slopes in the switching time – voltage diagram are all very similar in a range of 40–240 mV/dec. In addition, the device stack exhibits only a single slope except for the TiN/HfO_x/TiN cells of Ielmini et al. (red open squares), the HfO_x data published by Cao et al. (red filled circles), and $SrTiO_3$ data of Fleck (black open squares). However, most of the studies only cover less than five orders of magnitude in switching time and another slope might appear if more orders of magnitude are investigated. The extracted slopes seem to correlate with the specific oxide material irrespective of the used metal electrodes, that is, ≈170 mV/dec for HfO_x-based VCM cells, ≈240 mV/dec for TaO_x-based VCM cells, 50 mV/dec for TiO_x-based VCM cells, and 150 mV/dec for $SrTiO_3$ (STO)-based VCM cells. According to the switching mechanism discussed in Section 2.3 the migration of double–positively charged oxygen vacancies is expected to limit the switching speed. In order to explain the slopes by electric field acceleration of the ion transport, the voltage would have to drop over a distance of $w = 1.2 \cdot a$ for TiO_x, $w = 2.4 \cdot a$ for STO, $w = 3.0 \cdot a$ for HfO_x, and $w = 4.2 \cdot a$ for TaO_x devices, respectively. Considering a rather wide hopping distance a ≈ 0.5 nm, w needs to extend over no more than 0.6 nm – 2.1 nm in order to explain the slope by pure field acceleration.

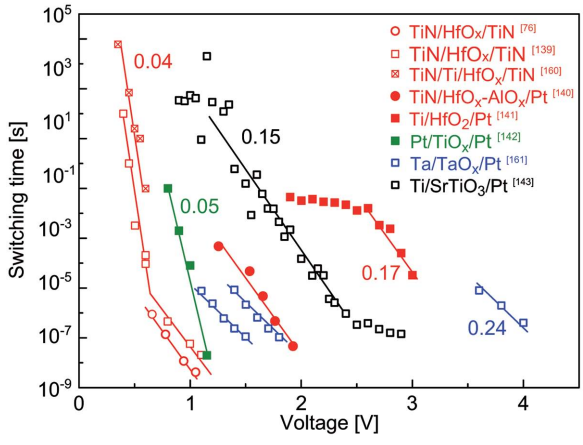

Figure 8. Switching kinetics data for VCM cells of hafnium oxide (red),[76,139–141,160] titanium oxide (green),[142] tantalum oxide (blue),[161] and strontium titanate (black).[143] A specific slope $\Delta V/\mathrm{dec}(t)$ of each oxide material can be identified in a narrow range. Shifts along the voltage axis for same species are related to an increase of the oxide thickness. For HfO_x and $SrTiO_x$-based cells regimes with different slopes are observed.

The transient currents prior to the abrupt SET operation are typically higher than μA and hence enough power is dissipated locally to heat up the device. Thus, it seems to be more likely that the ion migration is accelerated by a combination of electric field and local temperature increase due to Joule heating. In fact, it has been first demonstrated by Menzel et al. for a STO–based VCM cell using electro–thermal modeling in comparison with experimental data that temperature-acceleration of the ion hopping is the dominating factor in explaining the non-linear switching kinetics.[144] A further indication of the role of temperature appears in the switching kinetics data of Cao (red full circles) as well as in those of Fleck (black open squares). For low voltages the slope is very flat, but at higher voltages a sudden acceleration of switching speed sets in. As discussed in Section 3.6 this behavior cannot be explained by a second process limiting the switching speed. In that case the slope should become flatter for increasing voltages. This observed behavior, however, can be explained by the onset of Joule heating at a certain voltage. Typically, the *I*–*V* characteristic of the HRS is very non-linear, thus Joule heating can set in abruptly if enough power is dissipated within the device (cf. Menzel et al.)[144]

According to Equation (16) the local temperature increase due to Joule heating depends on the dissipated power in the device. Thus, a clear dependence of the switching time on the dissipated power should be expected if temperature–acceleration dominates. By analyzing the current transients Nishi and co-workers extracted the overall power dissipation in two 5 nm thick TaO_x based cells A and B (cf. **Figure 9**a).[125] In the switching time–voltage plot the data of the two cells is just shifted about 0.3 V. In contrast both data sets coincide if the switching time is plotted against the power as shown in Figure 9b. Thus, the Joule heating effect of the HRS leakage current is dominant in the SET mechanism. Furthermore, the power–dependence could also be demonstrated for measurements at room temperature and at 85 °C.[125] In this case, the acceleration of the switching speed at an elevated temperature is attributed to the increase of the HRS current.

Further evidence for the importance of Joule heating is given by Ielmini and co-workers. They developed a VCM switching model based on radial filamentary growth driven by an Arrhenius-type law and calculated the temperature increase during switching according to Equation (16). With this model the switching kinetics data of the TiN/HfO_x/TiN devices shown in Figure 8 could be reproduced over many orders of magnitude.[139] Using a kinetic Monte Carlo model Degraeve et al. could also reproduce the switching dynamics over several order of magnitudes.[145] The driving force of this non-linearity stems from the temperature accelerated hopping probability of defects between different reservoirs representing the conductive filament. The conductivity of the filament was described by a quantum point contact conduction model similar to the one proposed by Lian et al.[146] Recently, Fleck et al. developed an analytical model for the calculation of the SET switching time that can also explain the interrelation between pulse and sweep experiments for the STO-based VCM cell shown as black squares in Figure 8.[143] In this model the switching is estimated by the time an ion requires to migrate a certain distance l_{disc} following the approach of Menzel et al.[144] With the ion velocity according to the Mott–Gurney law of ion hopping the SET time is calculated by

$$t_{SET} = \frac{l_{disc}}{af}\exp\left(\frac{\Delta W_{hop}}{k_B T_{disc}}\right)\sinh\left(\frac{ea}{k_B T_{disc}}\cdot\frac{V_{disc}}{l_{disc}}\right) \quad (18)$$

The voltage V_{disc} resembles that part of the applied voltage dropping over a so-called disc region, in which the switching is assumed to take place (cf. **Figure 10**a). To calculate V_{disc} it is assumed that the current transport through the filament can be described by a non-linear (diode-like) disc resistance and an Ohmic resistance in series. The temperature in the disc region is then calculated according to Equation (16). The calculated SET times match the switching kinetics data obtained from pulse experiments on a Pt/STO/Ti VCM cell as illustrated in Figure 10b. To extend this model to sweep experiments, the voltage sweep was divided into discrete intervals with constant stepwise increasing voltage. For each voltage level the travelled distance is calculated according to Equation (18) and summed up until the sum equals l_{disc}. In this way the experimental SET sweep kinetics could be reproduced over several orders of magnitude as shown in Figure 10c.

As the resistive switching is explained in terms of the migration of oxygen vacancies, the retention of the programmed device states are governed by their redistribution due to diffusion processes. Noman et al. demonstrated by means of drift–diffusion simulations that the activation energy of ion diffusion should exceed 1.02 eV in order to achieve a 10 year retention.[115]

The switching kinetics data illustrated in Figure 8 often covers only a small voltage range and hence a limited switching time regime. However, for understanding the processes involved in resistive switching the whole voltage regime should be investigated. For example an additional slope might appear

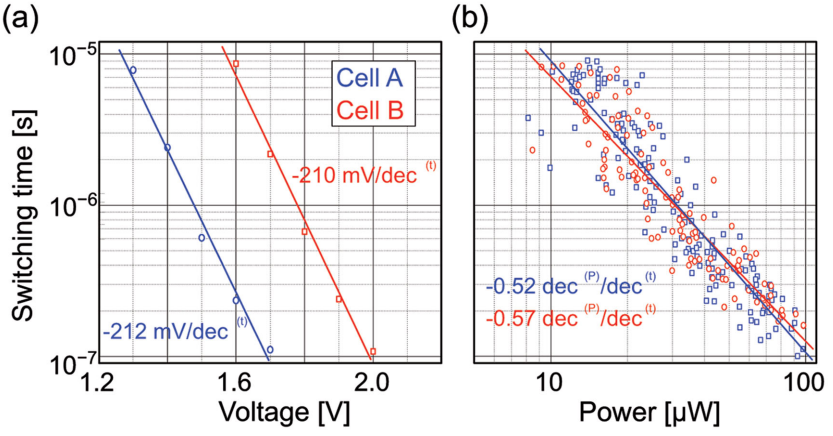

Figure 9. a) SET switching time vs applied voltage for different TaO_x-based VCM cells A (blue) and B (red). b) SET switching time plotted against the corresponding SET power extracted from the SET transients for both cells. While there is parallel shift in the t_{SET}-*V* data, the t_{SET}-*P* data coincide. Data are adopted from Nishi et al.[125]

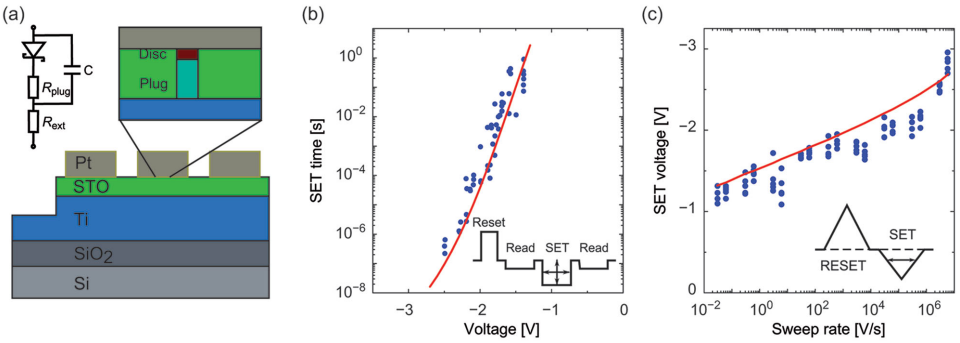

Figure 10. a) Schematic cross section and equivalent circuit of a STO-based VCM cell. b) Corresponding SET switching time as function of the applied voltage in experiment (blue) and obtained from model calculations (red). c) Switching voltage of the STO-based VCM cell measured as a function of the sweep-rate (blue) in comparison to the analytical model (red). Reproduced with permission.[143] Copyright 2014, IEEE.

at lower voltages being a fingerprint for another limiting physical process. With respect to the solution of the voltage–time dilemma it has been demonstrated that the resistive switching can be as fast as several 100 ps in a TaO_x based VCM cell.[7] Furthermore, Ninomiya et al. demonstrated stable SET and RESET switching using 10 ns pulses for 10^5 cycles in a 1-Kb 1T1R Ir/TaO_x/Ta_2O_5/TaN array.[147] In addition, the HRS and LRS state showed stable retention behavior over 100 h at 175°C. To achieve this device stability the authors tuned the composition of the TaO_x layer and such a way that a smaller filament is formed in the Ta_2O_5 layer.[148] Fantini et al. could demonstrate that alloying HfO_2 with moderate amounts of Al_2O_3 improves the LRS retention by lowering the oxygen vacancy diffusivity and activation energy.[149] This is in agreement with the theoretical discussion in Section 3.

4.3. Phase-Change Memories

The switching speed in phase-change memories is mainly limited by the SET process and the involved crystallization kinetics. Studies on amorphous thin films can provide valuable insights into crystal nucleation and growth in phase change materials. However, it is important to keep in mind that the situation in the SET process in nano-structured vertical phase-change devices can be different. In these vertical cells the amorphous plug is typically surrounded by crystalline phase-change material. Therefore, a crystalline-amorphous interface is always present in the HRS of nano-structured devices. A study by Bruns et al. indicated that crystallization speed in various phase-change materials, such as GeTe, $Ge_2Sb_2Te_5$, doped Sb_2Te and $Ge_3Sn_1Te_4$, is strongly dependent on the size of the amorphous region, which is represented by the device resistance (see **Figure 11**).[9,35,150]

With increasing device resistance (and plug size) the minimal pulse duration for full crystallization increases. This can be understood as experimental evidence for a growth-dominated crystallization process. Waiting for a spontaneous formation of supercritical nuclei is not necessary, which accelerates the total process of crystallization. Measurements on amorphous AgIn-doped Sb_2Te that had been melt-quenched with a laser, revealed a purely growth-dominated crystallization process starting at the rim of the amorphous spots at the interface to the crystalline surrounding all the way to the center (over spot radii of several 100 nm).[37] The investigated samples showed an activation energy for crystallization of 2.7 eV within a temperature range between 418 K and 553 K. While at low temperatures (≈420 K) the growth velocity was found to be in the range of 100 nm/s, it is strongly enhanced to more than 3 m/s at the upper temperature limit of the experimental range. In a recent work of Sebastian et al. the crystal growth velocity in doped $Ge_2Sb_2Te_5$ was measured over a temperature regime starting at 160 °C up to 270 °C in mushroom type memory cells.[151] An Arrhenius behavior spanning over eight orders of magnitude was found for the growth velocity. For doped $Ge_2Sb_2Te_5$ an activation energy for crystallization of 3.01 eV was determined. Both of the studies on thin films and nano-structured devices proved the pronounced non-linearity in crystallization kinetics. This

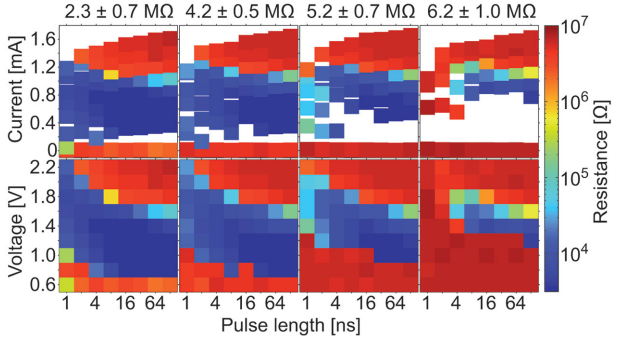

Figure 11. Crystallization speed of a vertical GeTe-mushroom cell programmed in four different initial high resistance states (columns). The color code shows how much the device resistance changed upon an excitation with a particular voltage pulse. In the bottom row, this resistance change is plotted dependent on the voltage and the duration of the applied set pulse. The top row additionally illustrates the dependence of this resistance change on the maximum current passing through the device during the pulsed electrical excitation. Each voltage pulse had sharp edges of 2 ns. While a reduction in cell resistance is visible for currents below 0.9 mA, reamorphization takes place at higher currents (larger than 1.1 mA). Crystallization can only occur when a minimal voltage (the threshold voltage) is exceeded (transition from red to blue data points). The comparison of experiments with four different initial RESET states reveals an increasing threshold voltage with device resistance (which is representative for the size of the amorphous region), indicating the field-driven nature of threshold switching. Reproduced with permission.[9] Copyright 2009, AIP.

characteristic fingerprint of phase-change materials is essential in overcoming the voltage-time dilemma of resistive memories.

Besides the strong non-linearity in crystallization kinetics, the stability of the HRS (amorphous state) also benefits from the non-linear *I–V* characteristics of the amorphous material. Before any crystallization via Joule heating can take place, the reversible transition from the amorphous "OFF-" to the "ON-state", the threshold switching, has to occur. Therefore, switching speed and retention of phase change memories are also determined by the threshold-switching phenomenon. Performing experiments on as-deposited amorphous lateral phase-change cells it has been shown that threshold switching happens, when a critical electrical field is exceeded.[152] The absolute value of this critical field is sensitive to the chosen pulse parameters and to the phase-change material under test.

While delay times for threshold switching (**Figure 12**a) have been studied for almost 50 years now,[112,153–158] new insights were reported very recently.[159] In this work, experimental evidence for an accumulative effect towards threshold switching was shown. Before the abrupt breakdown in resistivity, a continuous and linear increase in current ("pre-switching-slope", preSS) can be observed in case of sufficiently high electrical fields. For low field strength no increase in current and also no switching event occurs. At a critical electrical field the preSS deviates from zero and foretells the occurrence of the threshold switching effect (Figure 12b). Thereby, a minimal electrical field for threshold switching can be experimentally determined for phase-change memories. The existence of such a minimal field ensures a high stability of the cell state during read-out and strengthens the data retention in amorphous phase-change materials.

While the threshold switching delay time was extensively studied as a function of applied voltage and cell resistance, the influence of ambient temperature is rarely characterized.[104,112,157] In the few existing works a general trend of switching at lower voltages was found for increasing temperatures.

Revisiting the mechanisms described above, the voltage-time dilemma in phase-change materials is cooperatively solved by the non-linear current–voltage characteristics including the effect of threshold switching as well as by the unique crystallization kinetics. At voltages well above the minimal electrical field for switching, the threshold switching event can be triggered within nanoseconds (or even less)[36] and the extremely large crystal growth velocities (>1 m/s) enable an ultra-fast SET process for this class of material. At low voltages, below the minimal threshold field, good data retention is guaranteed over long time scales due to the high activation energies that need to be overcome for crystallization.

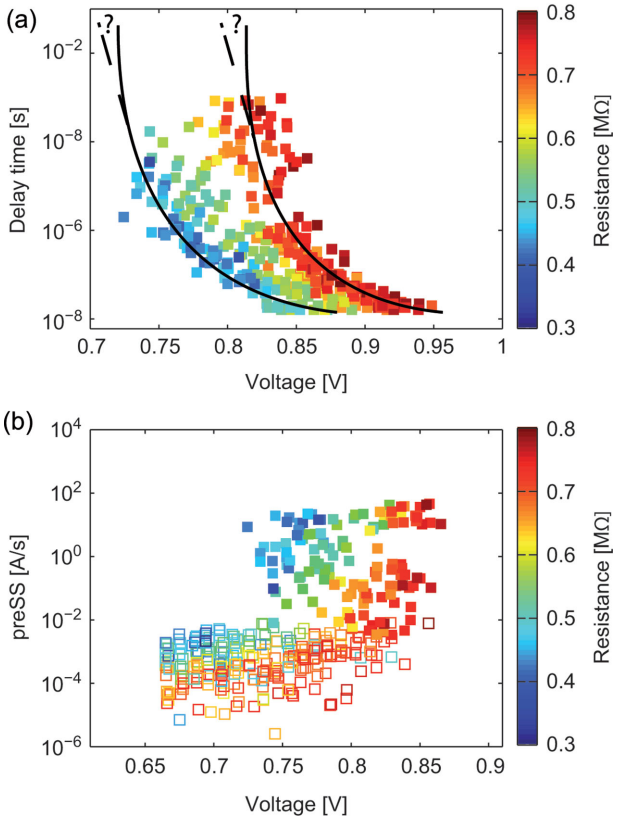

Figure 12. a) Threshold switching delay time as a function of applied voltage for cells with varying initial amorphous plug size (i.e., initial resistance). In order to investigate the delay time for different amorphous plug sizes, the amplitude of the preceding reset pulse was varied, resulting in cell resistances between 300 and 800 kΩ. In agreement with an electric-field-induced switching-mechanism a decrease in initial cell resistance, and thus a decrease in amorphous thickness between effective electrodes, results in a lowering of the voltages, at which threshold switching takes place after a specific delay time. Although, delay times were measured over five orders of magnitude in time the existence of a minimal threshold field cannot be proven based on such an analysis alone. b) Pre-switching-slope as a function of applied voltage measured for various initial cell resistances between 300 and 800 kΩ. Filled squares indicate the existence of a threshold-switching event during the applied pulse, whereas unfilled symbols represent experiments, in which no switching event occurred. The device resistance shows a pronounced influence on the voltage dependent pre-switching-slope. For smaller initial resistances the curves are shifted towards lower voltages. Because a smaller initial resistance is indicative of a smaller size of the initial amorphous plug, this shift of curves is in line with the increase in current prior to threshold-switching being an effect induced by the electric field. Reproduced with permission.[159] Copyright 2014, IOP.

5. Conclusions

In summary, we presented voltage-dependent resistive switching time data for PCM, VCM, and ECM cells and we discussed the underlying physical and (electro-)chemical mechanisms, such as crystallization including nucleation and growth of a new phase, threshold switching, ion migration, interface-related electron-transfer reactions, and electro-crystallization. It was shown that different effects are limiting the switching speed depending on the voltage strength resulting in a strong *V–t* non-linearity.

The processes in ECM cells could be identified using an analytical switching model describing cylindrical filament growth in the switching layer and modulation of the tunneling gap between the filament and the active electrode. Electro-crystallization dominates the low voltage switching behavior,

whereas with increasing voltage electron-transfer reactions and later ion migration limit the switching kinetics.

In VCM devices, in which resistive switching is explained in terms of the migration of oxygen vacancies, an electrothermal model enabled the successful simulation of experimental data. At low voltages the migration is field-accelerated, at high voltages the process is determined by the considerable temperature increase in the switching regions due to Joule heating, leading to a pronounced non-linearity of the switching kinetics.

In PCM materials, the switching from the amorphous to the crystalline state occurs only above a threshold voltage. Reversible threshold switching generates Joule heating which initiates irreversible crystallization with extremely large crystal growth velocities resulting in ultra-fast resistive switching. In case of low voltages the resistive state remains unaffected.

In conclusion, we can state that the described PCM, VCM, and ECM devices show a sufficiently strong non-linearity with respect to their switching kinetics and have thus the potential to overcome the voltage-time dilemma.

Acknowledgements

This work was supported by the Deutsche Forschungsgemeinschaft under Grant SFB 917.

Received: March 2, 2015
Revised: May 8, 2015
Published online: June 18, 2015

[1] R. Waser, R. Dittmann, G. Staikov, K. Szot, *Adv. Mater.* **2009**, *21*, 2632.
[2] I. Valov, M. N. Kozicki, *J. Phys. D Appl. Phys.* **2013**, *46*, 074005.
[3] J. J. Yang, D. B. Strukov, D. R. Stewart, *Nat. Nanotechnol.* **2013**, *8*, 13.
[4] S. Raoux, D. Ielmini, M. Wuttig, I. Karpov, *MRS Bull.* **2012**, *37*, 118.
[5] H.-S. P. Wong, H.-Y. Lee, S. Yu, Y.-S. Chen, Y. Wu, P.-S. Chen, B. Lee, F. T. Chen, M.-J. Tsai, *Proc. IEEE* **2012**, *100*, 1951.
[6] M. Meier, C. Schindler, S. Gilles, R. Rosezin, A. Rudiger, C. Kügeler, R. Waser, *IEEE Electron Device Lett.* **2009**, *30*, 8.
[7] A. C. Torrezan, J. P. Strachan, G. Medeiros-Ribeiro, R. S. Williams, *Nanotechnology* **2011**, *22*, 485203/1.
[8] C. Hermes, M. Wimmer, S. Menzel, K. Fleck, G. Bruns, M. Salinga, U. Boettger, R. Bruchhaus, T. Schmitz-Kempen, M. Wuttig, R. Waser, *IEEE Electron Device Lett.* **2011**, *32*, 1116.
[9] G. Bruns, P. Merkelbach, C. Schlockermann, M. Salinga, M. Wuttig, T. D. Happ, J. B. Philipp, M. Kund, *Appl. Phys. Lett.* **2009**, *95*, 43108/1.
[10] S. Lai, *IEEE Int. Electron Devices*, IEEE, Pisacataway, NJ, USA **2003**.
[11] M. N. Kozicki, M. Park, M. Mitkova, *IEEE Trans. Nanotechnol.* **2005**, *4*, 331.
[12] M.-J. Lee, C. B. Lee, D. Lee, S. R. Lee, M. Chang, J. H. Hur, Y.-B. Kim, C.-J. Kim, D. H. Seo, S. Seo, U.-I. Chung, I.-K. Yoo, K. Kim, *Nat. Mater.* **2011**, *10*, 625.
[13] I. S. Kim, S. L. Cho, D. H. Im, E. H. Cho, D. H. Kim, G. H. Oh, D. H. Ahn, S. O. Park, S. W. Nam, J. T. Moon, C. H. Chung, *2010 Symposium On VLSI Technology, Digest of Technical Papers* **2010**, 203.
[14] V. V. Zhirnov, R. K. Cavin, S. Menzel, E. Linn, S. Schmelzer, D. Bräuhaus, C. Schindler, R. Waser, *Proc. IEEE* **2010**, *98*, 2185.
[15] V. V. Zhirnov, R. Meade, R. K. Cavin, G. Sandhu, *Nanotechnology* **2011**, *22*, 254027/1.
[16] Samsung (press release), Samsung Announces Production Start-up of its Next-generation Nonvolatile Memory PRAM http://www.samsung.com/global/business/semiconductor/news-events/press-releases/detail?newsId=4097 (accessed: December 2014).
[17] Panasonic (press release), Panasonic Starts World's First Mass Production of ReRAM Mounted Microcomputers, http://panasonic.co.jp/corp/news/official.data/data.dir/2013/07/en130730–2/en130730–2.html (accessed: December 2014)
[18] R. Fackenthal, M. Kitagawa, W. Otsuka, K. Prall, D. Mills, K. Tsutsui, J. Javanifard, K. Tedrow, T. Tsushima, Y. Shibahara, G. Hush, *IEEE International Solid-State Circuits Conference Digest of Technical Papers* **2014**, 338.
[19] J. Borghetti, G. S. Snider, P. J. Kuekes, J. J. Yang, D. R. Stewart, R. S. Williams, *Nature* **2010**, *464*, 873.
[20] M. Cassinerio, N. Ciocchini, D. Ielmini, *Adv. Mater.* **2013**, *25*, 5975.
[21] E. Linn, R. Rosezin, S. Tappertzhofen, U. Böttger, R. Waser, *Nanotechnology* **2012**, *23*, 305205.
[22] D. Loke, J. M. Skelton, W.-J. Wang, T.-H. Lee, R. Zhao, T.-C. Chong, S. R. Elliott, *Proc. Natl. Acad. Sci. U.S.A.* **2014**, *111*, 13272.
[23] M. Wuttig, N. Yamada, *Nat. Mater.* **2007**, *6*, 824.
[24] D. Lencer, M. Salinga, M. Wuttig, *Adv. Mater.* **2011**, *23*, 2030.
[25] S. K. Bahl, K. L. Chopra, *J. Appl. Phys.* **1970**, *41*, 2196.
[26] R. G. Neale, J. A. Aseltine, *IEEE Trans. Electron Devices* **1973**, *ED20*, 195.
[27] N. Yamada, E. Ohno, K. Nishiuchi, N. Akahira, M. Takao, *J. Appl. Phys.* **1991**, *69*, 2849.
[28] S. C. Moss, J. P. DeNeufville, *J. Non-Cryst. Solids* **1972**, *8–10*, 45.
[29] P. Chaudhari, S. R. Herd, *J. Non-Cryst. Solids* **1972**, *8–10*, 56.
[30] M. Chen, K. A. Rubin, R. W. Barton, *Appl. Phys. Lett.* **1986**, *49*, 502.
[31] M. Libera, M. Chen, *J. Appl. Phys.* **1993**, *73*, 2272.
[32] N. Ohshima, *J. Appl. Phys.* **1996**, *79*, 8357.
[33] J. H. Coombs, A. P. J. M. Jongenelis, W. van EsSpiekman, B. A. J. Jacobs, *J. Appl. Phys.* **1995**, *78*, 4906.
[34] V. Weidenhof, N. Pirch, I. Friedrich, S. Ziegler, M. Wuttig, *J. Appl. Phys.* **2000**, *88*, 657.
[35] G. Bruns, *PhD thesis*, RWTH Aachen, January **2012**.
[36] D. Loke, T. H. Lee, W. J. Wang, L. P. Shi, R. Zhao, Y. C. Yeo, T. C. Chong, S. R. Elliott, *Science* **2012**, *336*, 1566.
[37] M. Salinga, E. Carria, A. Kaldenbach, M. Bornhoefft, J. Benke, J. Mayer, M. Wuttig, *Nat. Commun.* **2013**, *4*, 2371/1.
[38] J. Orava, A. L. Greer, B. Gholipour, D. W. Hewak, C. E. Smith, *Nat. Mater.* **2012**, *11*, 279.
[39] D. Ielmini, Y. Zhang, *J. Appl. Phys.* **2007**, *102*, 054517.
[40] Y. H. Shih, M. H. Lee, M. Breitwisch, R. Cheek, H. L. Lung, C. Lam, *10th IEEE Int. Conf. Solid-State and Integrated Circuit Technology* **2010**.
[41] R. Waser, M. Aono, *Nat. Mater.* **2007**, *6*, 833.
[42] G. Palma, E. Vianello, G. Molas, C. Cagli, F. Longnos, J. Guy, M. Reyboz, C. Carabasse, M. Bernard, F. Dahmani, D. Bretegnier, J. Liebault, B. De Salvo, *Jpn. J. Appl. Phys.* **2013**, *52*, UNSP 04CD02/1.
[43] J. R. Jameson, N. Gilbert, F. Koushan, J. Saenz, J. Wang, S. Hollmer, M. N. Kozicki, *Appl. Phys. Lett.* **2011**, *99*, 063506.
[44] R. Soni, P. Meuffels, A. Petraru, O. Vavra, H. Kohlstedt, *J. Appl. Phys.* **2013**, *113*, 124504/1.
[45] S. Tappertzhofen, I. Valov, R. Waser, *Nanotechnology* **2012**, *23*, 145703.
[46] S. Menzel, S. Tappertzhofen, R. Waser, I. Valov, *Phys. Chem. Chem. Phys.* **2013**, *15*, 6945.
[47] T. Tsuruoka, T. Hasegawa, I. Valov, R. Waser, M. Aono, *AIP Adv.* **2013**, *3*, 32114/1.
[48] C. Schindler, G. Staikov, R. Waser, *Appl. Phys. Lett.* **2009**, *94*, 072109/1.

[49] Y. Bernard, V. T. Renard, P. Gonon, V. Jousseaume, *Microelectron. Eng.* **2011**, *88*, 814.
[50] I. Valov, *ChemElectroChem* **2014**, *1*, 26.
[51] M. Kund, G. Beitel, C. U. Pinnow, T. Roehr, J. Schumann, R. Symanczyk, K. D. Ufert, G. Mueller, *IEDM Tech. Dig.* **2005**, 754.
[52] C. Schindler, *PhD thesis*, RWTH Aachen, January **2009**
[53] S. Menzel, U. Böttger, R. Waser, *J. Appl. Phys.* **2012**, *111*, 014501/1.
[54] T. Tsuruoka, T. Hasegawa, K. Terabe, M Aono, *Nanotechnology* **2012**, *23*, 435705.
[55] J. R. Jameson, N. Gilbert, F. Koushan, J. Saenz, J. Wang, S. Hollmer, M. Kozicki, N. Derhacobian, *IEEE Electron Device Lett.* **2012**, *33*, 257.
[56] S. Tappertzhofen, E. Linn, S. Menzel, A. J. Kenyon, R. Waser, I. Valov, *IEEE Trans. Nanotechnol.* **2015**, *14*, 505.
[57] T. Tsuruoka, K. Terabe, T. Hasegawa, M. Aono, *Nanotechnology* **2010**, *21*, 425205/1.
[58] W. Guan, S. Long, Q. Liu, M. Liu, W. Wang, *IEEE Electron Device Lett.* **2008**, *29*, 434.
[59] C. Schindler, S. C. P. Thermadam, R. Waser, M. N. Kozicki, *IEEE Trans. Electron Devices* **2007**, *54*, 2762.
[60] S. Menzel, N. Adler, J. van den Hurk, S. Tappertzhofen, I. Valov, R. Waser, *5th IEEE Int. Memory Workshop* **2013**, 92.
[61] U. Celano, L. Goux, A. Belmonte, K. Opsomer, A. Franquet, A. Schulze, C. Detavernier, O. Richard, H. Bender, M. Jurczak, W. Vandervorst, *Nano Lett.* **2014**, *14*, 2401.
[62] U. Celano, L. Goux, A. Belmonte, G. Giammaria, K. Opsomer, C. Detavernier, O. Richard, H. Bender, F. Irrera, M. Jurczak, W. Vandervorst, IEEE Int. Electron Devices Meeting, San Franicsco, CA **2014**.
[63] S. Tappertzhofen, H. Mündelein, I. Valov, R. Waser, *Nanoscale* **2012**, *4*, 3040.
[64] D. Y. Cho, S. Tappertzhofen, R. Waser, I. Valov, *Nanoscale* **2013**, *5*, 1781.
[65] K. Terabe, T. Hasegawa, T. Nakayama, M. Aono, *Nature* **2005**, *433*, 47.
[66] I. Valov, I. Sapezanskaia, A. Nayak, T. Tsuruoka, T. Bredow, T. Hasegawa, G. Staikov, M. Aono, R. Waser, *Nat. Mater.* **2012**, *11*, 530.
[67] A. Nayak, T. Tamura, T. Tsuruoka, K. Terabe, S. Hosaka, T. Hasegawa, M. Aono, *J. Phys. Chem. Lett.* **2010**, *1*, 604.
[68] A. Nayak, T. Tsuruoka, K. Terabe, T. Hasegawa, M. Aono, *Nanotechnology* **2011**, *22*, 235201/1.
[69] Y. Yang, P. Gao, L. Li, X. Pan, S. Tappertzhofen, S. Choi, R. Waser, I. Valov, W. D. Lu, *Nat. Commun.* **2014**, *5*, 4232/1.
[70] K. Szot, W. Speier, G. Bihlmayer, R. Waser, *Nat. Mater.* **2006**, *5*, 312.
[71] C. Lenser, M. Patt, S. Menzel, A. Köhl, C. Wiemann, C. M. Schneider, R. Waser, R. Dittmann, *Adv. Funct. Mater.* **2014**, *24*, 4466.
[72] S. Lee, J. S. Lee, J.-B. Park, Y. K. Kyoung, M.-J. Lee, T. W. Noh, *APL Mater.* **2014**, *2*, 066103.
[73] M. D. Pickett, D. B. Strukov, J. L. Borghetti, J. J. Yang, G. S. Snider, D. R. Stewart, R. S. Williams, *J. Appl. Phys.* **2009**, *106*, 074508.
[74] D. S. Jeong, H. Schroeder, R. Waser, *Electrochem. Solid State Lett.* **2007**, *10*, G51.
[75] S. Yu, H.-Y. Chen, B. Gao, J. Kang, H.-S. P. Wong, *ACS Nano* **2013**, *7*, 2320.
[76] S. Koveshnikov, K. Matthews, K. Min, D. Gilmer, M. Sung, S. Deora, H. Li, S. Gausepohl, P. Kirsch, R. Jammy, *Technical Digest – Int. Electron Devices* **2012**, 20.4.1.
[77] D. Lee, J. Woo, E. Cha, S. Park, S. Lee, J. Park, H. Hwang, *IEEE Electron Device Lett.* **2013**, *34*, 1250.
[78] H. Zhang, N. Aslam, M. Reiners, R. Waser, S. Hoffmann-Eifert, *Chem. Vapor Deposition* **2014**, *20*, 282.
[79] J. J. Yang, M. D. Pickett, X. Li, D. A. A. Ohlberg, D. R. Stewart, R. S. Williams, *Nat. Nanotechnol.* **2008**, *3*, 429.
[80] Y. B. Nian, J. Strozier, N. J. Wu, X. Chen, A. Ignatiev, *Phys. Rev. Lett.* **2007**, *98*, 146403/1.
[81] R. Waser, R. Bruchhaus, S. Menzel, *Nanoelectronics and Information Technology, 3rd ed.*, Wiley-VCH, Weinheim, Germany **2012**, 683.
[82] J. J. Yang, F. Miao, M. D. Pickett, D. A. A. Ohlberg, D. R. Stewart, C. N. Lau, R. S. Williams, *Nanotechnology* **2009**, *20*, 215201.
[83] D.-H. Kwon, K. M. Kim, J. H. Jang, J. M. Jeon, M. H. Lee, G. H. Kim, X.-S. Li, G.-S. Park, B. Lee, S. Han, M. Kim, C. S. Hwang, *Nat. Nanotechnol.* **2010**, *5*, 148.
[84] R. J. Kamaladasa, A. A. Sharma, Y. Lai, W. Chen, P. A. Salvador, J. A. Bain, M. Skowronski, Y. N. Picard, *Microsc. Microanal.* **2015**, *21*, 140.
[85] G. Bersuker, D. C. Gilmer, D. Veksler, P. Kirsch, L. Vandelli, A. Padovani, L. Larcher, K. McKenna, A. Shluger, V. Iglesias, M. Porti, M. Nafria, *J. Appl. Phys.* **2011**, *110*, 124518/1.
[86] S. Yu, X. Guan, H. Wong, *IEEE Trans. Electron Devices* **2012**, *59*, 1183.
[87] B. Gao, S. Yu, N. Xu, L. F. Liu, B. Sun, X. Y. Liu, R. Q. Han, J. F. Kang, B. Yu, Y. Y. Wang, *IEEE Int. Electron Devices 2008, Technical Digest* **2008**, 563.
[88] S. Clima, B. Govoreanu, M. Jurczak, G. Pourtois, *Microelectron. Eng.* **2014**, *120*, 13.
[89] A. O'Hara, G. Bersuker, A. A. Demkov, *J. Appl. Phys.* **2014**, *115*, 183703.
[90] K. Xue, B. Traore, P. Blaise, L. Fonseca, E. Vianello, G. Molas, B. De Salvo, G. Ghibaudo, B. Magyari-Kope, Y. Nishi, *IEEE Trans. Electron Devices* **2014**, *61*, 1394.
[91] M. Bocquet, D. Deleruyelle, H. Aziza, C. Muller, J. M. Portal, T. Cabout, E. Jalaguier, *IEEE Trans. Electron Devices* **2014**, *61*, 674.
[92] V. Weidenhof, I. Friedrich, S. Ziegler, M. Wuttig, *J. Appl. Phys.* **2001**, *89*, 3168.
[93] B. J. Kooi, J. T. M. De Hosson, *J. Appl. Phys.* **2004**, *95*, 4714.
[94] B. J. Kooi, W. M. G. Groot, J. T. M. De Hosson, *J. Appl. Phys.* **2004**, *95*, 924.
[95] C. V. Thompson, F. Spaepen, *Acta Metall.* **1979**, *27*, 1855.
[96] M. D. Ediger, *Annu. Rev. Phys. Chem.* **2000**, *51*, 99.
[97] M. Salinga, *PhD thesis*, RWTH Aachen, June **2008**.
[98] J. W. Christian, *Theory of Transformations in Metals and Alloys*, 2nd ed, Pergamon, New York **1975**.
[99] G. W. Burr, P. Tchoulfian, T. Topuria, C. Nyffeler, K. Virwani, A. Padilla, R. M. Shelby, M. Eskandari, B. Jackson, B.-S. Lee, *J. Appl. Phys.* **2012**, *111*, 104308/1.
[100] S. R. Ovshinsky, *Phys. Rev. Lett.* **1968**, *21*, 1450.
[101] R. W. Pryor, *Appl. Phys. Lett.* **1971**, *18*, 324.
[102] H. K. Henisch, R. W. Pryor, G. J. Vendura, *J. Non-Cryst. Solids* **1972**, *8–10*, 415.
[103] D. M. Kroll, *Physical Review B* **1974**, *9*, 1669.
[104] S. H. Lee, H. K. Henisch, *J. Non-Cryst. Solids* **1972**, *11*, 192.
[105] A. Pirovano, A. L. Lacaita, A. Benvenuti, F. Pellizzer, R. Bez, *IEEE Trans. Electron Devices* **2004**, *51*, 452.
[106] A. Redaelli, A. Pirovano, A. Benvenuti, A. L. Lacaita, *J. Appl. Phys.* **2008**, *103*, 111101/1.
[107] V. G. Karpov, Y. A. Kryukov, I. V. Karpov, M. Mitra, *Phys. Rev. B: Condens. Matter* **2008**, *78*, 52201/1.
[108] R. M. Hill, *Phil. Mag.* **1971**, *23*, 59.
[109] T. Stubb, T. Suntola, O. J. A. Tianien, *Solid-State Electron.* **1972**, *15*, 611.
[110] J. M. Marshall, *Solid-State Electron.* **1973**, *16*, 629.
[111] D. Adler, M. S. Shur, M. Silver, S. R. Ovshinsky, *J. Appl. Phys.* **1980**, *51*, 3289.
[112] V. G. Karpov, Y. A. Kryukov, M. Mitra, I. V. Karpov, *J. Appl. Phys.* **2008**, *104*, 054507.

[113] D. B. Strukov, R. S. Williams, *Appl. Phys. A-Mater. Sci. Process.* **2009**, *94*, 515.
[114] S. Yu, H.-S. Wong, *IEEE Trans. Electron Devices* **2011**, *58*, 1352.
[115] M. Noman, W. Jiang, P. A. Salvador, M. Skowronski, J. A. Bain, *Appl. Phys. A – Mater. Sci. Process.* **2011**, *102*, 877.
[116] P. Meuffels, H. Schroeder, *Appl. Phys. A Mater. Sci. Process.* **2011**, *105*, 65.
[117] G. Staikov, *Electrocrystallization in Nanotechnology*, Wiley-VCH, Weinheim, Germany **2007**.
[118] E. Budevski, G. Staikov, W. J. Lorenz, *Electrochemical Phase Formation and Growth*, VCH, Weinheim, Germany **1996**.
[119] R. Soni, P. Meuffels, G. Staikov, R. Weng, C. Kuegeler, A. Petraru, M. Hambe, R. Waser, H. Kohlstedt, *J. Appl. Phys.* **2011**, *110*, 54509/1.
[120] I. Valov, G. Staikov, *J. Solid State Electrochem.* **2013**, *17*, 365.
[121] Y. M. Lu, M. Noman, Y. N. Picard, J. A. Bain, P. A. Salvador, M. Skowronski, *J. Appl. Phys.* **2013**, *113*, 163703/1.
[122] P. Sun, L. Li, N. Lu, Y. Li, M. Wang, H. Xie, S. Liu, M. Liu, *J.Comput. Electron.* **2014**, *13*, 432.
[123] B. Govoreanu, S. Clima, I. Radu, Y. Chen, D. Wouters, M. Jurczak, *IEEE Trans. Electron Devices* **2013**, *60*, 2471.
[124] S. Kim, S. Choi, W. Lu, *ACS Nano* **2014**, *8*, 2369.
[125] Y. Nishi, S. Menzel, K. Fleck, U. Boettger, R. Waser, *IEEE Electron Device Lett.* **2014**, *35*, 259.
[126] A. Belmonte, W. Kim, B. T. Chan, N. Heylen, A. Fantini, M. Houssa, M. Jurczak, L. Goux, *IEEE Trans. Electron Devices* **2013**,*60*, 3690 .
[127] D. Kamalanathan, U. Russo, D. Ielmini, M. N. Kozicki, *IEEE Electron Device Lett.* **2009**, *30*, 553.
[128] U. Russo, D. Kamalanathan, D. Ielmini, A. L. Lacaita, M. N. Kozicki, *IEEE Trans. Electron Devices* **2009**, *56*, 1040.
[129] L. Gao, S. B. Lee, B. Hoskins, H. K. Yoo, B. S. Kang, *Appl. Phys. Lett.* **2013**, *103*, 43503/1.
[130] T. Tsuruoka, K. Terabe, T. Hasegawa, M. Aono, *Nanotechnology* **2011**, *22*, 254013.
[131] S. Tappertzhofen, I. Valov, T. Tsuruoka, T. Hasegawa, R. Waser, M. Aono, *ACS Nano* **2013**, *7*, 6396.
[132] S. Tappertzhofen, R. Waser, I. Valov, *ChemElectroChem* **2014**, *1*, 1287.
[133] A. Pinkowski, T. Chierchie, W. Lorenz, *J. Electroanal. Chem. Interfacial Electrochem.* **1990**, *285*, 241.
[134] S. Menzel, B. Wolf, S. Tappertzhofen, I. Valov, U. Böttger, R. Waser, *6th IEEE Int. Memory Workshop,*Taipeh, Taiwan **2014**.
[135]Stefan Tappertzhofen, *RWTH Aachen University* **2014**.
[136] A. Calderoni, S. Sills, N. Ramaswamy, *6th IEEE Int. Memory Workshop,*Taipeh, Taiwan **2014**, 5.
[137] L. Goux, K. Opsomer, A. Franquet, G. Kar, N. Jossart, O. Richard, D. J. Wouters, R. Muller, C. Detavernier, M. Jurczak, J. A. Kittl, *Thin Solid Films* **2013**, *533*, 29.
[138] J. Guy, G. Molas, P. Blaise, C. Carabasse, M. Bernard, A. Roule, G. Le Carval, V. Sousa, H. Grampeix, V. Delaye, A. Toffoli, J. Cluzel, P. Brianceau, O. Pollet, V. Balan, S. Barraud, O. Cueto, G. Ghibaudo, F. Clermidy, B. De Salvo, L. Perniola, *IEEE International Electron Devices Meeting* **2014**, 6.5.
[139] D. Ielmini, F. Nardi, S. Balatti, *IEEE Trans. Electron Devices* **2012**, *59*, 2049.
[140] S. Yu, Y. Wu, H. Wong, *Appl. Phys. Lett.* **2011**, *98*, 103514/1.
[141] M. G. Cao, Y. S. Chen, J. R. Sun, D. S. Shang, L. F. Liu, J. F. Kang, B. G. Shen, *Appl. Phys. Lett.* **2012**, *101*, 203502/1.
[142] F. Alibart, L. Gao, B. D. Hoskins, D. B. Strukov, *Nanotechnology* **2012**, *23*, 75201/1.
[143] K. Fleck, U. Böttger, R. Waser, S. Menzel, *IEEE Electron Device Lett.* **2014**, *35*, 924.
[144] S. Menzel, M. Waters, A. Marchewka, U. Böttger, R. Dittmann, R. Waser, *Adv. Funct. Mater.* **2011**, *21*, 4487.
[145] R. Degraeve, A. Fantini, N. Raghavan, Y. Y. Chen, L. Goux, S. Clima, S. Cosemans, B. Govoreanu, D. J. Wouters, Ph. Roussel, G. S. Kar, G. Groeseneken, M. Jurczak, *Proc. 2013 Symp. VLSI Technology* **2013**.
[146] X. Lian, X. Cartoixa, E. Miranda, L. Perniola, R. Rurali, S. Long, M. Liu, J. Sune, *J. Appl. Phys.* **2014**, *115*, 244507.
[147] T. Ninomiya, S. Muraoka, Z. Wei, R. Yasuhara, K. Katayama, T. Takagi, *IEEE Electron Device Lett.* **2013**, *34*, 762.
[148] T. Ninomiya, Z. Wei, S. Muraoka, R. Yasuhara, K. Katayama, T. Takagi, *IEEE Trans. Electron Devices* **2013**, *60*, 1384.
[149] A. Fantini, L. Goux, S. Clima, R. Degraeve, A. Redolfi, C. Adelmann, G. Polimeni, Y. Y. Chen, M. Komura, A. Belmonte, D. J. Wouters, M. Jurczak, 6th IEEE Int. Memory Workshop, Taipeh, Taiwan, **2014**.
[150] J. Luckas, A. Piarristeguy, G. Bruns, P. Jost, S. Grothe, R. M. Schmidt, C. Longeaud, M. Wuttig, *J. Appl. Phys.* **2013**, *113*, 23704/1.
[151] A. Sebastian, M. Le Gallo, D. Krebs, *Nat. Commun.* **2014**, *5*, 4314/1.
[152] D. Krebs, S. Raoux, C. T. Rettner, G. W. Burr, M. Salinga, M. Wuttig, *Appl. Phys. Lett.* **2009**, *95*, 82101/1.
[153] R. R. Shanks, *J. Non-Cryst. Solids* **1970**, *2*, 504.
[154] S. H. Lee, H. K. Henisch, W. D. Burgess, *J. Non-Cryst. Solids* **1972**, *8–10*, 422.
[155] D. Adler, H. K. Henisch, N. Mott, *Rev. Mod. Phys.* **1978**, *50*, 209.
[156] D. H. Kang, B. Cheong, J. Jeong, T. S. Lee, I. H. Kim, W. M. Kim, J. Y. Huh, *Appl. Phys. Lett.* **2005**, *87*, 253504/1.
[157] S. Lee, D. S. Jeong, J.-H. Jeong, W. Zhe, Y.-W. Park, H.-W. Ahn, B.-.K. Cheong, *Appl. Phys. Lett.* **2010**, *96*, 23501/1.
[158] S. Lavizzari, D. Sharma, D. Ielmini, *IEEE Trans. Electron Devices* **2010**, *57*, 1047.
[159] M. Wimmer, M. Salinga, *N. J. Phys.* **2014**, *16*, 113044.
[160] T. Diokh, E. Le-Roux, S. Jeannot, M. Gros-Jean, P. Candelier, J. F. Nodin, V. Jousseaume, L. Perniola, H. Grampeix, T. Cabout, E. Jalaguier, M. Guillermet, B. De Salvo, *2013 IEEE Int. Reliability Physics Symp.* **2013**, 5E.4.1.
[161] Y. Nishi, S. Schmelzer, U. Böttger, R. Waser, *Proc. 43rd European Solid-State Device Research Conf.* **2013**, 174.